



Cite this: *Phys. Chem. Chem. Phys.*,
2020, 22, 27496

The role of electron–nuclear coupling on multi-state photoelectron spectra, scattering processes and phase transitions†

Joy Dutta,‡ Soumya Mukherjee,‡ Koushik Naskar, Sandip Ghosh, Bijit Mukherjee, Satyam Ravi and Satrajit Adhikari *

We present first principle based beyond Born–Oppenheimer (BBO) theory and its applications on various models as well as realistic spectroscopic and scattering processes, where the Jahn–Teller (JT) theory is brought in conjunction with the BBO approach on the phase transition of lanthanide complexes. Over one and half decades, our development of BBO theory is demonstrated with *ab initio* calculations on representative molecules of spectroscopic interest (NO_2 radical, Na_3 and K_3 clusters, NO_3 radical, C_6H_6^+ and $1,3,5\text{-C}_6\text{H}_3\text{F}_3^+$ radical cations) as well as triatomic reactive scattering processes ($\text{H}^+ + \text{H}_2$ and $\text{F} + \text{H}_2$). Such an approach exhibits the effect of JT, Renner–Teller (RT) and pseudo Jahn–Teller (PJT) type of interactions. While implementing the BBO theory, we generate highly accurate diabatic potential energy surfaces (PESs) to carry out quantum dynamics calculation and find excellent agreement with experimental photoelectron spectra of spectroscopic systems and cross-sections/rate constants of scattering processes. On the other hand, such electron–nuclear couplings incorporated through JT theory play a crucial role in dictating higher energy satellite transitions in the dielectric function spectra of the LaMnO_3 complex. Overall, this article thoroughly sketches the current perspective of the BBO approach and its connection with JT theory with various applications on physical and chemical processes.

Received 30th July 2020,
Accepted 20th October 2020

DOI: 10.1039/d0cp04052e

rsc.li/pccp

1 Introduction

The fundamental theoretical framework of Born–Oppenheimer (BO) treatment^{1,2} appears to be the cornerstone for studying chemical processes over almost a century. Despite the fact that the BO approximation is successful to depict some of the ground state chemical processes, its breakdown is quite frequent due to significant electron–nuclear (nonadiabatic) coupling among the ground and other excited electronic states. Such phenomena quite often occur in nature, namely, photosynthesis, vision, solar energy conversions *etc.*^{3–8} The interactions among the electronic states are crucial at the degenerate or near-degenerate point(s)/ seam(s) over the nuclear configuration space (CS), where the nonadiabatic coupling terms (NACTs) show a singular feature as depicted by Hellmann–Feynman theorem.^{9,10} As a result, while extracting spectral profiles of a molecule or dynamical quantities of a chemical reaction, significant anomalies are observed between the results obtained from single and multiple surface calculations.^{11–13} Therefore, a paradigm shift on electronic structure as well as

dynamical calculations to beyond the Born–Oppenheimer (BBO) domain is inevitable to incorporate the contribution of higher electronic states even for a ground state molecular process.

The Jahn–Teller (JT) theorem¹⁴ introduced in the late thirties of the last century reveals that any nonlinear molecule possessing degenerate electronic state would undergo a geometrical distortion to lower its overall energy. Van Vleck¹⁵ first explored this phenomenon by solving an $\mathbf{E} \otimes \mathbf{e}$ problem for an octahedral complex ($\text{M.6H}_2\text{O}$, M is paramagnetic metal ion). Later on, Longuet-Higgins, Öpik and Pryce^{16,17} calculated eigenvalues and eigenfunctions for the lower sheet of the doubly-branched ‘Mexican hat’ potential energy surface (PES) of electron–nuclear coupled JT active systems containing d^4 and d^9 metal ions (*e.g.*, Mn^{3+} and Cu^{2+}). Furthermore, O’Brien¹⁸ investigated the effect of anharmonicity on the lower sheet of such PES within adiabatic approximation. On the other hand, Slonczewski¹⁹ unveiled the existence of centrifugally stabilized excited state resulting from the coupling between linear JT and centrifugal forces. Recently, Dutta *et al.*²⁰ has explored the effect of anharmonicity, *i.e.*, cubic perturbation on the centrifugally stabilized excited state of the LaMnO_3 complex and investigated the origin of higher energy narrow satellite transitions exhibiting anomalous temperature dependence in the domain of Néel temperature, $T_N \simeq 140$ K.^{21–24}

School of Chemical Sciences, Indian Association for the Cultivation of Science, Jadavpur, Kolkata 700032, India. E-mail: pcsa@iacs.res.in

† Electronic supplementary information (ESI) available. See DOI: [10.1039/d0cp04052e](https://doi.org/10.1039/d0cp04052e)
 ‡ J. Dutta and S. Mukherjee contributed equally to this work.

The Longuet-Higgins treatment of the JT model depicts that the adiabatic BO eigenfunction attains a phase and undergoes sign inversion while traversing along a closed path encircling a degenerate point over the nuclear CS.^{25,26} Such multivalued property of those eigenfunctions was corrected by Herzberg and Longuet-Higgins in an *ad hoc* way²⁷ by incorporating a complex phase factor, familiar as Longuet-Higgins phase. In an alternative approach, Mead and Truhlar²⁸ circumvented this deficiency of the multivalued nuclear wavefunction by introducing a vector potential in the nuclear kinetic energy operator, where this new potential is reminiscent of the Longuet-Higgins phase. Varandas *et al.*²⁹ and later on, Adhikari *et al.*³⁰ calculated adiabatic BO electronic eigenfunctions considering triatomic molecules (LiNaK and Na_3) and demonstrated the sign inversion of the dominant coefficient of the eigenfunction along a closed loop encapsulating a conical intersection (CI). Althorpe *et al.*^{31–35} led an extensive investigation on the effects of the aforementioned phase in the dynamical studies for the ground electronic state^{31–33} and later on, this approach was employed involving upper electronic states to investigate population transfer³⁴ and state-to-state dynamics³⁵ at energies higher than the minimum energy of CI (MECI).

It is well accepted that the adiabatic PESs are physically meaningful. On the contrary, in the same representation, the singular nature of NACTs at the degenerate point(s) over the nuclear CS brings numerical inaccuracies during dynamical calculations. Thereby, it is necessary to recast the adiabatic nuclear Schrödinger equation (SE) to a different one (diabatic), where the singular kinetic couplings are transformed into smooth and continuous terms. Such transformation is known as adiabatic-to-diabatic transformation (ADT). Hobey and McLachlan³⁶ first employed the ADT technique to construct a potentially coupled (diabatic) framework for a single degree of freedom (DOF) and later on, the same formulation was implemented by F. T. Smith³⁷ on a diatomic molecule. While exploring the atom–diatom collision reactions, M. Baer formulated a set of coupled differential equations to diabatize the adiabatic PESs and NACTs for a given sub-Hilbert space (SHS),^{3,38,39} which are numerically solved along a two-dimensional contour over the nuclear CS. It is worthwhile to highlight that the existence and uniqueness of those solutions is asserted if the NACT vector fields fulfil the curl condition^{39,40} for a given SHS. If the required number of electronic states forming the sub-space are incorporated in ADT calculation, the computed mixing (ADT) angles result in an integer (n) multiple of $\pi^{39,41,42}$ along a closed loop enclosing degenerate point(s) or passing through a seam. On the other hand, Mead *et al.*^{28,43} predicted that ADT can at best eliminate the longitudinal component (removable part) of NACTs, which blows up in the vicinity of a conical intersection (CI) or seam,⁴⁴ but the magnitude of the transverse component (non-removable part) is generally negligible at those regions or can be made negligible by expanding the nuclear CS and/or the sub-Hilbert space. Subsequently, various diabatization methods have been proposed (see Subsection 6.1 for details), namely vibronic coupling model (VCM),^{45–58} exact factorisation (EF)^{59–61} scheme, direct dynamical approaches^{62–66} and also other methods,^{67–70} but the first principle based

approach developed by M. Baer^{3,38–42} is considered as one of the most accurate ones.

In later works, Adhikari *et al.* generalized the BBO theory for three to six coupled electronic states with rigorous formulation of NACT expressions, ADT equations, curl-divergence equations and diabatic potential energy matrix elements.^{30,71–84} Recently, our group developed an algorithm and user-friendly OpenMP parallelized program for ADT,⁸⁵ which can be highly useful for deriving analytic expressions of various ADT quantities (like ADT equations, ADT matrix elements, diabatic potential energy matrix elements, *etc.*) and also for evaluating numerical solutions of those quantities. Apart from the generalization of BBO theory, successful attempts are made to formulate the single surface extended Born–Oppenheimer (EBO) equations^{71,86,87} for non-Abelian cases ($N \geq 3$) by employing the curl condition. In addition, we have implemented molecular symmetry (MS) adaptation to correct the signs of NACTs at different regions of nuclear CS as predicted by the corresponding irreducible representation (IRREP) of the MS group of that molecule or molecular process.^{30,74} It is needless to say that such operation enables us to generate a totally symmetric (A) diabatic PES matrix. Since this first principle based ADT formalism leads to single-valued, continuous and smooth diabatic PESs as well as couplings, this approach is expected to reproduce the experimental outcomes both for spectroscopic^{30,74,76,77,80–84,87–89} and scattering processes^{75,78,79,84,89–91} involving multiple electronic states. Such systems/processes not only exhibit diverse complexities in electronic structure but also possess a variety of nonadiabatic effects, namely, Jahn–Teller (JT),¹⁴ Renner–Teller (RT)⁹² and pseudo Jahn–Teller (PJT)⁹³ interactions. Our group has computed diabatic PESs of alkali trimers (Na_3 , K_3),^{30,74} nitrogen oxides (NO_2 , NO_3),^{77,82} benzene radical cations (C_6H_6^+) and 1,3,5-trifluorobenzene radical cations ($1,3,5\text{-C}_6\text{H}_3\text{F}_3^+$)⁸³ followed by quantum dynamical calculations, which has successfully reproduced the experimental photo-electron spectra.^{94–98} Moreover, we have been implementing the BBO theory to generate diabatic surfaces of H_3^{+75} and $\text{F} + \text{H}_2^{79,91}$ systems to compute reactive cross sections and rate constants. The diabatic PESs of H_3^+ in hyperspherical coordinates^{75,78} have been employed to study the multisurface reactive scattering dynamics on a $\text{D}^+ + \text{H}_2$ system,⁹⁰ and the calculated reaction probabilities and integral cross-sections (ICS) are in excellent accordance with the experimental findings.⁹⁹ In a similar way, we are carrying out reactive scattering calculations on $\text{F} + \text{H}_2$ using the highly accurate diabatic PESs^{79,91} (incorporating spin-orbit couplings) and the computed dynamical quantities (cross-sections and rate constants) are expected to show satisfactory agreement with previous theoretical results.¹⁰⁰

The aim of this article is to present a concise overview of our theoretical developments and applications of the BBO approach as well as its connection with JT theory, which is expected to be helpful for the associated scientific community. This article focusses on the theoretical background of several aspects of BBO theory, followed by implementation of current methodology in spectroscopic systems as well as triatomic scattering processes. In addition, the development of JT theory and its application are also explored with a detailed analysis on the phase transition of

rare earth metal complexes. Finally, the accuracy of our theoretical results is compared with the available experimental as well as other theoretical findings.

2 Born–Oppenheimer treatment

While discussing BBO theory, we demonstrate the formulation of first principle based BO treatment,¹ which was developed employing a double perturbative approach. Since the total electron–nuclear Hamiltonian dictates the molecular properties, we can commence with the following time-independent SE,

$$\hat{H}(\mathbf{r}, \mathbf{R})\Psi(\mathbf{r}, \mathbf{R}) = E\Psi(\mathbf{r}, \mathbf{R}), \quad (1)$$

where \mathbf{r} and \mathbf{R} collectively represent the electronic and nuclear coordinate vectors, respectively. The molecular Hamiltonian [$\hat{H}(\mathbf{r}, \mathbf{R})$] can be segregated into nuclear kinetic energy operator [$\hat{T}_{\text{nuc}}(\mathbf{R})$] and electronic Hamiltonian [$\hat{H}_{\text{el}}(\mathbf{r}; \mathbf{R})$] as follows,

$$\hat{H}(\mathbf{r}, \mathbf{R}) = \hat{T}_{\text{nuc}}(\mathbf{R}) + \hat{H}_{\text{el}}(\mathbf{r}, \mathbf{R}), \quad (2)$$

where in this treatment, $\hat{T}_{\text{nuc}}(\mathbf{R}) \left[= -\sum \frac{\hbar^2}{2M} \left(\frac{\partial^2}{\partial \mathbf{R}^2} \right) \right]$ is considered as a perturbation on the electronic Hamiltonian [$\hat{H}_{\text{el}}(\mathbf{r}; \mathbf{R})$] due to large mass difference between electrons (m_e) and nuclei (M). When the electronic Hamiltonian, $\hat{H}_{\text{el}}(\mathbf{r}; \mathbf{R})$ and its eigenfunctions, $\xi_n(\mathbf{r}; \mathbf{R})$ s are expanded in Taylor series around a reference nuclear geometry (\mathbf{R}^0) at the close vicinity of \mathbf{R} [$\kappa \mathbf{x} (= \mathbf{R} - \mathbf{R}^0)$ denotes deviation in nuclear coordinate], the expressions of $\hat{H}_{\text{el}}(\mathbf{r}; \mathbf{R})$ and $\xi_n(\mathbf{r}; \mathbf{R})$ take the following form:

$$\hat{H}_{\text{el}}(\mathbf{r}; \mathbf{R}) = \hat{H}_{\text{el}}^0(\mathbf{r}; \mathbf{R}^0) + \kappa \hat{H}_{\text{el}}^1(\mathbf{r}; \mathbf{x}) + \kappa^2 \hat{H}_{\text{el}}^2(\mathbf{r}; \mathbf{x}) + \dots \quad (3)$$

$$\xi_n(\mathbf{r}; \mathbf{R}) = \xi_n^{(0)}(\mathbf{r}; \mathbf{R}^0) + \kappa \xi_n^{(1)}(\mathbf{r}; \mathbf{x}) + \kappa^2 \xi_n^{(2)}(\mathbf{r}; \mathbf{x}) + \dots \quad (4)$$

where $\kappa = \left(\frac{m_e}{M_0} \right)^{1/4}$, m_e and M_0 are electronic and mean nuclear masses, respectively.

At first, the perturbation is employed on the electronic Hamiltonian at the reference geometry, $\hat{H}_{\text{el}}^0(\mathbf{r}; \mathbf{R}^0)$ to evaluate order by order corrections on unperturbed eigenvalues and eigenfunctions at another nuclear configuration, $\hat{H}_{\text{el}}(\mathbf{r}; \mathbf{R})$. Secondly, the nuclear kinetic energy operator [$\hat{T}_{\text{nuc}}(\mathbf{R})$] acts as a perturbation on $\hat{H}_{\text{el}}(\mathbf{r}; \mathbf{R})$ to evaluate the similar corrections. After performing such double perturbations [see Section S1 in the ESI†] up to second order and comparing the two sets of perturbative solutions, the molecular wavefunction for the n th state can be expressed as a product of two series given by,

$$\begin{aligned} \Psi_n(\mathbf{r}, \mathbf{R}) &= [\psi_n^0(\mathbf{R}) + \kappa^1 \psi_n^1(\mathbf{R}) + \kappa^2 \psi_n^2(\mathbf{R}) + \dots] \\ &\quad [\xi_n^0(\mathbf{r}; \mathbf{R}^0) + \kappa \xi_n^1(\mathbf{r}; \mathbf{x}) + \kappa^2 \xi_n^2(\mathbf{r}; \mathbf{x}) + \dots] \quad (5) \\ &= \psi_n^{\text{ad}}(\mathbf{R}) \xi_n^{\text{ad}}(\mathbf{r}; \mathbf{R}) \end{aligned}$$

Thus, the total molecular wavefunction appears as a product of the nuclear and electronic wavefunction, where the first factor describes the nuclear component and the second one depicts the electronic contribution parametrically dependent on nuclear geometry. If corrections beyond second order are taken into account, the total molecular wavefunction can not be presented

as a product of the nuclear and electronic wavefunction due to cross additional terms. It may be noted that the molecular wavefunction for the n th state (see eqn (5)) is accurate up to κ^4 order. On the other hand, while incorporating the contribution of excited states, we can employ the Born–Oppenheimer–Huang (BOH) expansion² $\left[\Psi(\mathbf{r}, \mathbf{R}) = \sum_{n=1}^N \Psi_n(\mathbf{r}, \mathbf{R}) = \sum_{n=1}^N \psi_n^{\text{ad}}(\mathbf{R}) \xi_n^{\text{ad}}(\mathbf{r}; \mathbf{R}) \right]$ to represent the configuration space accurately.

3 Jahn–Teller theory

Jahn–Teller (JT) interactions¹⁴ are omnipresent in nature starting from small floppy molecules, namely, NO_3 ^{80,82} to rare earth metal complexes, like, LaMnO_3 ^{20,101,102} leading to the breakdown of the BO approximation (see Sections 2 and 4).^{1,2} According to JT theorem,¹⁴ any nonlinear molecule with degenerate electronic states exhibits geometrical distortion and removes the degeneracy in order to lower the overall energy of the species. While exploring such distortion, the electronic Hamiltonian can be expanded along the nuclear coordinates ($\{Q_k\}$) as,

$$\hat{H} = \hat{H}^0 + \sum_k \hat{V}_k Q_k + \frac{1}{2} \sum_{kl} \hat{V}_{kl} Q_k Q_l + \dots, \quad (6)$$

where \hat{H}^0 refers to the electronic Hamiltonian at equilibrium nuclear configuration ($\{Q_k\} = 0$). On the other hand, the coefficients of first and second order perturbations with respect to normal modes are denoted by $\hat{V}_k \left(= \frac{\partial H}{\partial Q_k} \right)$ and $\hat{V}_{kl} \left(= \frac{\partial^2 H}{\partial Q_k \partial Q_l} \right)$, respectively. The aforementioned first order term [eqn (6)] takes the following form in matrix elements,

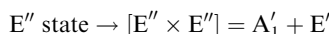
$$V_{ij} = \sum_k Q_k \langle \phi_i^{(0)} | \hat{V}_k | \phi_j^{(0)} \rangle, \quad (7)$$

where $\{\phi_n^{(0)}\}$ represents a complete set of degenerate electronic eigenfunctions. The above expression clearly depicts that a nonlinear molecule exhibits linear JT distortion (see Section S2 of the ESI†) along a normal mode coordinate if the integral, $\langle \phi_i^{(0)} | \hat{V}_k | \phi_j^{(0)} \rangle$ survives. In other words, the reducible representation of the product, $\Gamma(\phi_i^{(0)}) \otimes \Gamma(\hat{V}_k) \otimes \Gamma(\phi_j^{(0)})$ should possess the totally symmetric IRREP, Γ^0 . If the IRREPs of nuclear displacement (Q_k) and the degenerate electronic eigenfunctions are Γ^β and Γ^α , respectively, the necessary condition for the JT effect is given by,

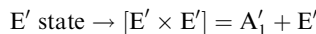
$$\Gamma^0 \in \Gamma^\beta \otimes [(\Gamma^\alpha)^2] \quad (8)$$

Hence, JT interaction can be observed only if the IRREP of Q_k is non-totally symmetric and is contained by the symmetrized direct product $[\Gamma^\alpha \times \Gamma^\alpha]$. In order to explore the validity of the JT condition [eqn (8)], we selectively choose one of the most intensely investigated molecules, NO_3 (D_{3h} system)^{80–82,103} and an analysis is presented in the following paragraphs. On the other hand, a brief discussion on the normal modes responsible for linear JT interaction in a model octahedral transition metal complex, $M\text{-}6\text{H}_2\text{O}$ (O_h)¹⁵ is demonstrated in Section S3 of the ESI† in view of symmetry arguments.

NO_3 manifests profound nonadiabatic interactions within the low-lying five electronic states, namely $\tilde{\text{X}}^2\text{A}'_2$, $\tilde{\text{A}}^2\text{E}''$ and $\tilde{\text{B}}^2\text{E}'$, which clusters within an energy gap of 2 eV at the equilibrium nuclear configuration. Among these five electronic states, $\tilde{\text{A}}^2\text{E}''$ (1^2A_2 and 1^2B_1) and $\tilde{\text{B}}^2\text{E}'$ (1^2A_1 and 2^2B_2) encounter JT interaction leading to lowering of symmetry and stabilization of their respective nether sheets, 1^2A_2 and 1^2A_1 by the e' vibrational modes, *i.e.*, along degenerate asymmetric stretching (Q_{3x} and Q_{3y}) and bending (Q_{4x} and Q_{4y}) modes.⁸² For this molecule, the reducible representations of the symmetrized direct products for $\tilde{\text{A}}^2\text{E}''$ and $\tilde{\text{B}}^2\text{E}'$ states are given by,



and



Since the degenerate Q_3 and Q_4 normal modes belong to e' symmetry (Γ^{β}), the JT condition (eqn (8)) takes the following form,

$$\text{e}' \otimes (\text{A}'_1 + \text{E}') \in \text{A}'_1. \quad (9)$$

As the resultant direct product contains the totally symmetric IRREP, A'_1 (symbolizing Γ^0), those modes can be considered as JT active modes. In contrast, totally symmetric Q_1 mode (a'_1) fulfills the JT condition [$\text{a}'_1 \otimes (\text{A}'_1 + \text{E}') \in \text{A}'_1$], but that is incapable of lifting the symmetry of the molecule *vis-à-vis* degeneracy. On the other hand, the umbrella mode (Q_2) belongs to a''_2 symmetry and hence, the direct product, $\text{a}''_2 \otimes (\text{A}'_1 + \text{E}')$ is devoid of A'_1 IRREP. Thus, the symmetry analysis clearly depicts that the modes (Q_1 and Q_2) are JT inactive. The atomic displacements for each vibrational mode and the character table of the D_{3h} point group along with the symmetry of the normal modes of NO_3 radical are presented in Section S4 of the ESI† for the sake of completeness.

3.1 The linear Jahn Teller model: an $\text{E} \otimes \text{e}$ problem

Within the linear electron–nuclear coupled $\text{E} \otimes \text{e}$ model,¹⁶ the circular motion of singly or triply occupied E_g ($|x^2 - y^2\rangle; |3z^2 - r^2\rangle$) electrons (angular coordinate, θ) in d^4 with high spin occupation (Mn^{3+}) or d^9 transition metal ions (Cu^{2+}) is deformed by an elliptical perturbation due to doubly degenerate vibrational modes, $Q_2 (= \rho \sin \phi)$ and $Q_3 (= \rho \cos \phi)$ of e_g symmetry. As a consequence, the degenerate electronic state is split with eigenvalues, $\pm A\rho$ and a doubly branched ‘Mexican hat’ vibronic PES is formed (see Fig. 1) with the combination of harmonic bond vibrational energy $\left(\frac{1}{2}M\omega_{\text{b-vib}}^2\rho^2\right)$ (see Section S2 of the ESI†):

$$V_{\pm} = \pm A\rho + \frac{1}{2}M\omega_{\text{b-vib}}^2\rho^2, \quad (10)$$

where the lower sheet of the PES, *i.e.*, ground state is stabilized by JT energy, $E_{\text{JT}} = -\frac{A^2}{2M\omega_{\text{b-vib}}^2}$; the minimum – energy configurations (corresponding to $\frac{\partial V_-}{\partial \rho} = 0$) of the lower adiabatic potential

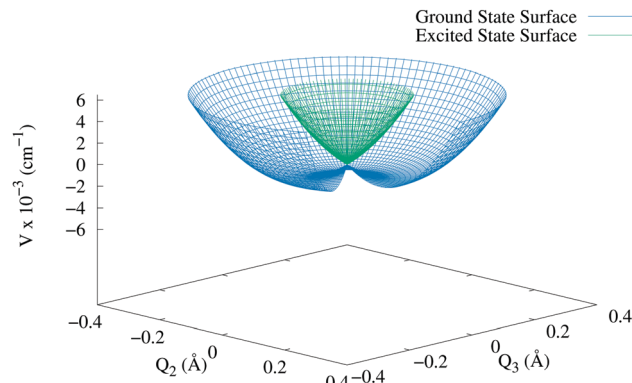


Fig. 1 Mexican Hat PES for the LaMnO_3 (rare earth orthorhombic manganite) complex.

energy surface (APES) are represented by a circular rim with radius, $|\rho_0^g| = \frac{A}{M\omega_{\text{b-vib}}^2}$; both the lower and upper sheet of APES have no barriers (V_{\pm} is independent of ϕ), thereby leading to spontaneous oscillations among different configurations, which is known as dynamic JT or the Longuet-Higgins–Öpik–Pryce–Sack (LHOPS) effect¹⁶.

Such elliptical perturbation¹⁶ ($H' = 2A\rho \cos(2\theta - \phi)$; θ and ϕ are electronic and nuclear angular coordinates, respectively) leads to the mixing of electronic and nuclear motion parametrically by allowing a vibronic interaction scheme, which results in the formation of pseudo – rotational states with quantum number, $l\left(=m+\frac{1}{2}\right)$ due to the coupling between vibrational (m) and electronic (j) angular quantum numbers. As a consequence, the radial vibronic SEs for lower and upper branches of the Mexican hat PES can be expressed as the following form under adiabatic approximation¹⁶ (see Subsection S2.1 of the ESI†):

$$-\frac{\hbar^2}{2M} \left[\frac{d^2\psi_g(\rho)}{d\rho^2} - \frac{l^2}{\rho^2}\psi_g(\rho) \right] - E^g\psi_g(\rho) \\ + \left(-A\rho + \frac{1}{2}M\omega_{\text{b-vib}}^2\rho^2 \right) \psi_g(\rho) = 0 \quad (11)$$

and

$$-\frac{\hbar^2}{2M} \left[\frac{d^2\psi_e(\rho)}{d\rho^2} - \frac{l^2}{\rho^2}\psi_e(\rho) \right] - E^e\psi_e(\rho) \\ + \left(A\rho + \frac{1}{2}M\omega_{\text{b-vib}}^2\rho^2 \right) \psi_e(\rho) = 0, \quad (12)$$

where $\psi_g(\rho)$ and $\psi_e(\rho)$ are the ground and excited state vibronic radial wavefunctions, respectively. The term $\frac{\hbar^2 l^2}{2M\rho^2}$ appearing in the above eqn (11) and (12) represents the pseudo – rotational energy with $l + \frac{1}{2}$ an integer arising from vibronic $\text{E}_g \otimes \text{e}_g$ interaction.

3.2 Motion of nuclei on the ground electronic state and the effect of anharmonicity

In the ground electronic state, the minima ($|\rho_0^g| = \frac{A}{M\omega_{b_vib}^2}$) are mainly formed due to two opposing forces, *i.e.*, linear Jahn-Teller ($F_{JT} = -A$) and harmonic bond vibrational ($F_{b_vib} = M\omega_{b_vib}^2\rho$), which appear away ($|\rho_0^g| = 0.3 \text{ \AA}^{17}$ for $[\text{Cu}(\text{H}_2\text{O})_6]^{2+}$ and $|\rho_0^g| = 0.21 \text{ \AA}^{20}$ for LaMnO_3 complex) from the center of APES and such states are called elastically stabilized vibronic states. As a result, centrifugal term $\frac{\hbar^2 l^2}{2M\rho^2}$ turns into a constant $\frac{\hbar^2 l^2}{2M\rho_0^2}$ at the minima ($\rho_0 = \frac{A}{M\omega_{b_vib}^2}$) of lower APES and the expression of eigenvalues takes the following form¹⁶ in terms of displaced harmonic oscillator at those minima within such approximation:

$$E_{pl}^g = \hbar\omega_{b_vib} \left(p + \frac{1}{2} \right) - \frac{A^2}{2M\omega_{b_vib}^2} + \frac{\hbar^2 l^2 M\omega_{b_vib}^4}{2A^2}, \quad (13)$$

$$p = 0, 1, 2, \dots$$

It is evident from eqn (13) that at the minima of the ground Mexican hat PES, nuclei exhibit roto-vibrational motions known as pseudo-rotations.

While incorporating higher order anharmonic term, $A_3\rho^3 \cos 3\phi^{17}$ breaks the infinite degeneracy of the ground electronic state, since the lower sheet of APES (V_-) becomes dependent on the vibrational distortion coordinate (ϕ). Consequently, the corresponding SE turns into the following form¹⁸ (see Subsection S2.2 of the ESI†):

$$-\frac{\hbar^2}{2M} \left[\frac{\partial^2}{\partial\rho^2} + \frac{1}{\rho^2} \frac{\partial^2}{\partial\phi^2} \right] \xi_g(\rho, \phi) - E\xi_g(\rho, \phi) \\ + \left(-A\rho + \frac{1}{2}M\omega_{b_vib}^2\rho^2 + A_3\rho^3 \cos(3\phi) \right) \xi_g(\rho, \phi) = 0, \quad (14)$$

where E can be expressed as $E = \varepsilon_0^g + \varepsilon$; ε_0^g and ε are the displaced harmonic oscillator $\left(-A\rho + \frac{1}{2}M\omega_{b_vib}^2\rho^2 \right)$ and cubic perturbed centrifugal eigenvalues, respectively.

Such anharmonicity results in the warping of the ‘Mexican hat’ PES by creating three minima for $\phi = \frac{\pi}{3}, \pi, \frac{5\pi}{3}; A_3 > 0$ and $\phi = 0, \frac{2\pi}{3}, \frac{4\pi}{3}; A_3 < 0$ along with three consecutive barriers (see Fig. 2).

The profiles of cubic perturbed roto-vibrational eigenvalues, ε (see Fig. S1 of Subsection S2.2 in the ESI†) as a function of barrier parameter ($-A_3\rho_0^3$; ρ_0 is ground state minima) are obtained by solving a secular determinant of radially averaged angular SE (Mathieu equation of C_{3v} symmetry), which is derived from eqn (14) within adiabatic approximation¹⁸ (see Subsection S2.2 in the ESI†). With the creation of minima and barriers, the system can sensibly fall into one of such minima corresponding to a particular nuclear configuration at slow pseudo-rotational limit, which is known as the static JT effect.¹⁸

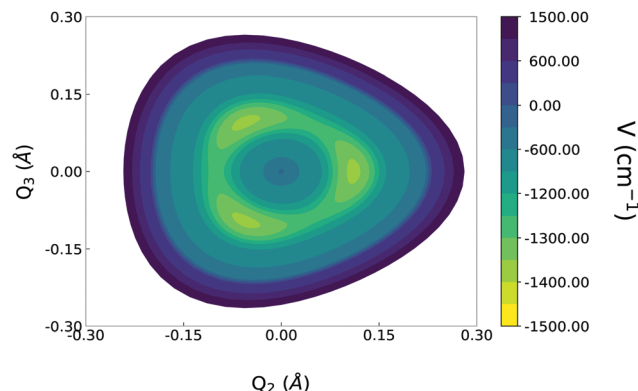


Fig. 2 Contour plot of lower sheet of cubic perturbed APES for the LaMnO_3 complex depicting three consecutive minima and barriers.

3.3 The theory of excited state: centrifugally stabilized cubic perturbed vibronic levels

The nuclear SE for the radial Hamiltonian of the upper sheet of APES can be written as (see eqn (12)):¹⁹

$$H\psi_e(\rho) = \left(-\frac{\hbar^2}{2M} \frac{\partial^2}{\partial\rho^2} + \frac{\hbar^2 l^2}{2M\rho^2} + A\rho + \frac{1}{2}M\omega_{b_vib}^2\rho^2 \right) \psi_e(\rho) \\ = E\psi_e(\rho), \quad (15)$$

where A and ω_{b_vib} are the linear Jahn-Teller term and bond vibrational frequency, respectively.

In contrast, the ground state with ‘Mexican hat’ PES, effect of centrifugal energy, $\frac{\hbar^2 l^2}{2M\rho^2}$ cannot be neglected in the excited state, since the linear Jahn-Teller ($A\rho$) term increases with ρ (contrast to the ground state) and gravitates the wave packet to be localized at the vicinity of $\rho \sim 0$, where the centrifugal energy $\frac{\hbar^2 l^2}{2M\rho^2}$ is of very large magnitude. In other words, the excited minima ($\{\rho_0^l\}$) are mainly formed due to two opposing forces, namely, centrifugal ($F_{\text{centrifugal}} = -\frac{\hbar^2 l^2}{M\rho^3}$) and linear Jahn-Teller ($F_{JT} = A$) ones, where the resulting bound states are called centrifugally stabilized vibronic states.¹⁹ The expression of minima and eigenvalues of the radial Hamiltonian for such centrifugally stabilized states (excluding bond vibration) take the following forms within harmonic approximation:¹⁹

$$\frac{\partial V_+}{\partial\rho} = -\frac{\hbar^2 l^2}{M\rho^3} + A = 0 \\ \rho_0^l = \left(\frac{\hbar^2 l^2}{AM} \right)^{\frac{1}{3}} \quad (16)$$

$$E_{s,l} \cong \frac{(\hbar A)^{2/3}}{M^{1/3}} \left[\frac{3}{2} |l|^{2/3} + \sqrt{3} \frac{\left(s + \frac{1}{2} \right)}{|l|^{1/3}} \right], \quad (17)$$

where $s = 0, 1, 2, \dots$ and $l = \pm\frac{1}{2}, \pm\frac{3}{2}, \pm\frac{5}{2}, \dots$ are the centrifugally stabilized vibrational and pseudo-rotational quantum numbers, respectively.

Incorporation of harmonic bond vibrational energy into the interaction Hamiltonian would lead to modulation of the centrifugally stabilized roto-vibrational states with the following elastically coupled oscillation frequency:²⁰

$$\Omega_l = \left[\frac{3A^{4/3}}{(\hbar|l|M)^{2/3}} + \omega_{\text{b-vib}}^2 \right]^{1/2}, \quad (18)$$

and the eigenvalues of such entangled states satisfy the following form:²⁰

$$E_{s,l}^{\text{b-vib}} = \frac{3(\hbar A|l|)^{2/3}}{2M^{1/3}} + \hbar \left[\frac{3A^{4/3}}{(\hbar|l|M)^{2/3}} + \omega_{\text{b-vib}}^2 \right]^{1/2} \left(s + \frac{1}{2} \right). \quad (19)$$

It is evident from eqn (17)–(19) that unlike usual oscillators, such centrifugally stabilized vibronic states are very much parametrically dependent on pseudo-rotational quantum number, l and thereby, leading to alteration of energy order of roto-vibrational levels in an interesting way (see Table S1 of Subsection S2.3 in the ESI†). Moreover, the singularity of energy spectrum located at $l = 0$ (see eqn (19)) emerges due to the cone PES of the centrifugally stabilized excited state.

The striking difference between the ground and excited electronic state is that in the upper sheet of the ‘Mexican hat’ APES, the centrifugal term contributes substantially, where the minima are determined by such centrifugal and linear Jahn-Teller forces (centrifugally stabilized state). As a result, determination of minima of cubic perturbed centrifugally stabilized vibronic states requires the entire spectrum of anharmonically perturbed pseudo-rotational energy on each grid point (ρ_i) of radial vibrational coordinate (ρ) [Dutta *et al.*²⁰]. Consequently, the nuclear SE of the cubic perturbed excited state:

$$\begin{aligned} & -\frac{\hbar^2}{2M} \left[\frac{\partial^2}{\partial \rho^2} + \frac{1}{\rho^2} \frac{\partial^2}{\partial \phi^2} \right] \xi_e(\rho, \phi) - E \xi_e(\rho, \phi) \\ & + \left(A\rho + \frac{1}{2} M \omega_{\text{b-vib}}^2 \rho^2 + A_3 \rho^3 \cos(3\phi) \right) \xi_e(\rho, \phi) = 0 \end{aligned} \quad (20)$$

has been averaged radially at every grid point ($\{\rho_i\}$) within adiabatic approximation, where $-\frac{\hbar^2}{2M\rho^2} \frac{\partial^2}{\partial \phi^2} + A_3\rho^3 \cos 3\phi$ represents the perturbation and the radial part ($w_e(\rho)$) of product type eigenfunction $\xi_e(\rho, \phi)$ ($= w_e^0(\rho)\gamma(\phi)$) is constrained to be at the lowest harmonic vibrational state $w_e^0(\rho)$. The corresponding angular SE (Mathieu equation) for each ρ grid point turns into:²⁰

$$\alpha_i \frac{\partial^2}{\partial \phi^2} \gamma(\phi) + \beta_i \cos(3\phi) \gamma(\phi) + \varepsilon(\rho_i) \gamma(\phi) = 0, \quad (21)$$

where both splitting α_i ($= \frac{\hbar^2}{2M\rho_i^2}$) and barrier β_i ($= -A_3\rho_i^3$) parameters become variables unlike for the ground state case (α ($= \frac{\hbar^2}{2M\rho_0^2}$); $\rho_0 \equiv$ ground state minima) is constant and β is the variable). The spectrum of $\varepsilon(\rho)$ is obtained by solving the

following secular equation of angular SE (eqn (21)) [employing $\gamma(\phi) = \sum_l a_l \exp(il\phi)$] at every grid point ($\{\rho_i\}$):

$$a_l (\varepsilon(\rho_i) - \alpha_i l^2) + \frac{1}{2} \beta_i (a_{l-3} + a_{l+3}) = 0. \quad (22)$$

Such cubic perturbed roto-vibrational energies ($\varepsilon(\rho)$) of various pseudo-rotational levels (l) establish bound states with the association of linear Jahn-Teller energy ($A\rho$) (see Fig. S2 of Subsection S2.4 in the ESI†). Thereby, the expression of cubic perturbed centrifugally stabilized excited state eigenvalues takes the following form within harmonic approximation (expanding V_+ ($= \varepsilon(\rho) + A\rho$) up to second order)²⁰ (see Table S2 of Subsection S2.4 in the ESI† for the numerical magnitude of eigenvalues):

$$E_{s,l}^{\text{cp}} = \varepsilon_l(\rho_0^l) + A\rho_0^l + \hbar \left[\frac{1}{M^{1/2}} \left(\frac{\partial^2 V_+}{\partial \rho^2} \right)_{\rho=\rho_0^l}^{\frac{1}{2}} \right] \left(s + \frac{1}{2} \right), \quad (23)$$

where ρ_0^l represents the minimum of cubic perturbed centrifugally stabilized excited state PES for particular pseudo-rotational level, l . Such cubic perturbed centrifugally stabilized oscillators are dressed with the bond vibration resulting elastically entangled roto-vibrational levels with the following eigenvalues²⁰ (see Table S3 of Subsection S2.4 in the ESI†):

$$E_{s,l}^{\text{cp+b-vib}} = \varepsilon_l(\rho_0^l) + A\rho_0^l + \hbar \left[\frac{1}{M} \left(\frac{\partial^2 V_+}{\partial \rho^2} \right)_{\rho=\rho_0^l} + \omega_{\text{b-vib}}^2 \right]^{\frac{1}{2}} \left(s + \frac{1}{2} \right), \quad (24)$$

where s and l represent the centrifugally stabilized elastically coupled vibrational and roto-vibrational quantum numbers, respectively.

4 Beyond Born–Oppenheimer theory

4.1 Adiabatic-to-diabatic transformation

The well known BOH expansion as depicted in Section 2^{1,2} allows the total molecular wavefunction [$\Psi(\mathbf{r}, \mathbf{R})$] for a N -dimensional SHS to be expressed as:

$$\Psi(\mathbf{r}, \mathbf{R}) = \sum_{i=1}^N \psi_i^{\text{ad}}(\mathbf{R}) \xi_i^{\text{ad}}(\mathbf{r}; \mathbf{R}), \quad (25)$$

where N number of electronic states are assumed to be non-adiabatically coupled with each other and decoupled from the remaining electronic manifold of a molecular system. In order to simplify our presentation, $\xi_i^{\text{ad}}(\mathbf{r}; \mathbf{R})$ is henceforth presented as $\xi_i(\mathbf{r}; \mathbf{R})$. In this expansion, $\{\xi_i(\mathbf{r}; \mathbf{R})\}_s$ are identified as the eigenfunctions of the electronic SE:

$$\hat{H}_{\text{el}}(\mathbf{r}; \mathbf{R}) \xi_i(\mathbf{r}; \mathbf{R}) = u_i(\mathbf{R}) \xi_i(\mathbf{r}; \mathbf{R}), \quad \langle \xi_i | \xi_j \rangle_{\mathbf{r}} = \delta_{ij}, \quad (26)$$

and the combining coefficients $\{\psi_i^{\text{ad}}(\mathbf{R})\}_s$ are the nuclear wavefunctions. In the electronic SE [eqn (26)], $\{u_i(\mathbf{R})\}_s$ define the adiabatic PESs and the integrals, $\langle \xi_i | \xi_j \rangle_{\mathbf{r}}$ are the inner product between two electronic states over electronic coordinates only.

While incorporating eqn (2), (25) and (26) in the time independent molecular SE (eqn (1)), we can arrive at the adiabatic

representation of nuclear SE in mass weighted dimensionless coordinate:

$$\sum_{j=1}^N \left(\hat{T}'_{ij}(\mathbf{R}) + (u_j(\mathbf{R}) - E) \delta_{ij} \right) \psi_j^{\text{ad}}(\mathbf{R}) = 0, \quad i = 1 \text{ to } N, \quad (27)$$

where $\hat{T}'_{ij}(\mathbf{R}) = \hat{T}_{\text{nuc}} \delta_{ij} - \frac{\hbar^2}{2} [2t_{ij}^{(1)}(\mathbf{R}) \cdot \nabla_R + t_{ij}^{(2)}(\mathbf{R})]$. In the above expression, $\hat{T}'_{ij}(\mathbf{R})$ and $U_{ij}(\mathbf{R}) (= u_j(\mathbf{R}) \delta_{ij})$ define nuclear kinetic and (adiabatic) potential energy operator matrix elements, respectively. On the other hand, $t_{ij}^{(1)}(\mathbf{R}) = \langle \xi_i | \nabla_R \xi_j \rangle_{\mathbf{r}}$ and $t_{ij}^{(2)}(\mathbf{R}) = \langle \xi_i | \nabla_R^2 \xi_j \rangle_{\mathbf{r}}$ are nonadiabatic coupling matrix (NACT) elements of first (vector field) and second (scalar field) kind, respectively. Moreover, using the orthogonality relation (eqn (26)) among the electronic states, it is possible to show that $t_{ij}^{(1)}(\mathbf{R})$ is a skew-symmetric matrix ($\langle \nabla_R \xi_i | \xi_j \rangle_{\mathbf{r}} = -\langle \xi_i | \nabla_R \xi_j \rangle_{\mathbf{r}}$) and then, it is related to $t_{ij}^{(2)}(\mathbf{R})$ in the following form:

$$\tau^{(2)}(\mathbf{R}) = \tau^{(1)}(\mathbf{R}) \cdot \tau^{(1)}(\mathbf{R}) + \nabla_R \cdot \tau^{(1)}(\mathbf{R}). \quad (28)$$

While substituting the aforementioned expression (eqn (28)) in eqn (27), we reach to the following compact form of adiabatic nuclear SE:

$$-\frac{\hbar^2}{2} (\nabla_R + \tau)^2 \psi^{\text{ad}} + (U - E) \psi^{\text{ad}} = 0, \quad (29)$$

In the following discussion, we have used τ instead of $\tau^{(1)}$ and functional dependence of τ , ψ^{ad} and U on the nuclear coordinates (\mathbf{R}) has been omitted.

On the other hand, the magnitude of NACTs encounters a steep rise (singular) at point(s) or along seam(s) of degeneracy between two electronic states, which is evident from the following expression:^{9,10}

$$\tau^{ij} = \frac{\langle \xi_i | \nabla_R \hat{H}_{\text{cl}} | \xi_j \rangle_{\mathbf{r}}}{u_j - u_i}. \quad (30)$$

The above equation (eqn (30)) clearly indicates the numerically inaccurate solution of kinetically coupled adiabatic SE at the close vicinity of degeneracy(ies) due to the singular vector functions, τ^{ij} . In order to get rid of this drawback of adiabatic representation, it is inevitable to introduce a new (diabatic) basis so that those singular terms are removed and consequently, well-behaved, smooth and single-valued potentially coupled SEs are generated. The transition from adiabatic to diabatic framework can be readily achieved by employing the transformation $\psi^{\text{ad}} = A \psi^{\text{dia}}$, where A is an orthogonal rotation matrix for a given sub-Hilbert space. While employing this relation, eqn (29) takes the following form:

$$\begin{aligned} & -\frac{\hbar^2}{2} [A \nabla_R^2 + 2(\nabla_R A + \tau A) \cdot \nabla_R + \{(\tau + \nabla_R) \cdot (\nabla_R A + \tau A)\}] \psi^{\text{dia}} \\ & + (U - E) A \psi^{\text{dia}} = 0, \end{aligned} \quad (31)$$

from which the singular vector functions (τ) can be removed under the following condition:

$$\nabla_R A + \tau A = 0, \quad (32)$$

known as the ADT condition.³⁸ This set of first order coupled differential equations are numerically integrated by substituting the *ab initio* calculated NACTs to evaluate the functional form of the A matrix elements. On imposing the ADT condition (eqn (32)) in eqn (31) and projecting with A^\dagger from the left, we achieve the diabatic representation of SE:

$$\left(-\frac{\hbar^2}{2} \nabla_R^2 + W - E \right) \psi^{\text{dia}} = 0, \quad W = A^\dagger U A, \quad (33)$$

where W is the diabatic potential energy matrix.

For N coupled electronic states, the model form of unitary matrix A is considered as a product of $A \left(= {}^N C_2 = \frac{N(N-1)}{2} \right)$ elementary rotational matrices constituted with sine and cosine functions of mixing angles between any two electronic states in that sub-Hilbert space, N . The elementary matrices can be arranged in $A!$ possible ways to form the A matrix:

$$A = P_n \{ A^{12}(\Theta_{12}) \cdot A^{13}(\Theta_{13}) \cdot A^{23}(\Theta_{23}) \cdot A^{14}(\Theta_{14}) \cdot \dots \cdot A^{N-1,N}(\Theta_{N-1,N}) \}, \quad n = 1, \dots, A!, \quad (34)$$

where P_n indicates the n th permutation between two rotational matrices and $\{\Theta_{ij}\}$ s represent the ADT angles, which are functions of nuclear coordinates. The elements of elementary matrices [$A^{mn}(\Theta_{mn})$] can be defined as:

$$\begin{aligned} [A^{mn}(\Theta_{mn})]_{mm} &= \cos \Theta_{mn} = [A^{mn}(\Theta_{mn})]_{nn} \quad m \neq n \\ [A^{mn}(\Theta_{mn})]_{nn} &= \sin \Theta_{mn} = -[A^{mn}(\Theta_{mn})]_{mm} \quad m \neq n \text{ and} \\ [A^{mn}(\Theta_{mn})]_{ij} &= \delta_{ij}; \quad \{i,j\} \neq \{m,n\} \end{aligned}$$

and a typical example of such matrix for a four-state SHS is:

$$A^{23}(\Theta_{23}) = \begin{pmatrix} 1 & 0 & 0 & 0 \\ 0 & \cos \Theta_{23} & \sin \Theta_{23} & 0 \\ 0 & -\sin \Theta_{23} & \cos \Theta_{23} & 0 \\ 0 & 0 & 0 & 1 \end{pmatrix}$$

While plugging the model form of the ADT matrix (eqn (34)) and skew-symmetric τ matrix in the ADT condition (eqn (32)), we obtain a set of A unique coupled linear differential equations involving the ADT angles Θ_{ij} , which can be generalized as:

$$\nabla_R \Theta_{ij} = \sum_{m=1}^A c^{(m)} \tau_{(m)}, \quad (35)$$

where the coefficients, $\{c^{(m)}\}$ s are scalar functions of mixing angles $\{\Theta_{kl}\}$. We present the explicit forms of ADT equations for three to five coupled electronic states in Section S5 of the ESI.† The *ab initio* calculated NACTs (τ^{kl}) are incorporated in eqn (35) and those equations are numerically integrated to compute the ADT angles $\{\Theta_{kl}\}$, where such angles are used to find the A matrices. Finally, those ADT matrices are employed in the similarity transformation (eqn (33)) to generate theoretically “exact” and numerically “accurate” smooth, single-valued and continuous diabatic PESs and couplings.

While diabatization by employing BBO theory, we first calculate the adiabatic PESs and the NACTs for a specific sub-Hilbert space of dimension, N . Prior to the diabatization through ADT, whether such space of dimension N truly forms a sub-Hilbert space within the accuracy of numerical calculation, we need to cross check the validity of two quantities at each point of the nuclear CS:

(a) Curl condition:

$$\frac{\partial \tau_q^{ij}}{\partial p} - \frac{\partial \tau_p^{ij}}{\partial q} = (\tau_q \tau_p)_{ij} - (\tau_p \tau_q)_{ij}, \quad (36)$$

where the Yang–Mills field (here, known as molecular field),

$$F_{pq}^{ij} = \left[\frac{\partial \tau_q^{ij}}{\partial p} - \frac{\partial \tau_p^{ij}}{\partial q} \right] - \left[(\tau_q \tau_p)_{ij} - (\tau_p \tau_q)_{ij} \right],$$

should be zero (0),

(b) Quantization of non-adiabatic coupling:

$$\int_0^{2\pi} \tau_\phi^{ij}(\rho, \phi) d\phi = n\pi, \quad (37)$$

where i, j are the two electronic states for a specific sub-Hilbert space [$\{i, j\} \in N\}$, p and q are Cartesian coordinates, ρ and ϕ are the polar transformed radial and circular coordinates, respectively associated with those Cartesian coordinates (p and q), τ_p^{ij} , τ_q^{ij} and τ_ϕ^{ij} (ρ, ϕ) are the scalar components of NACTs and n is the number of CIs. If both the conditions (eqn (36) and (37)) are numerically valid at a specific point of nuclear CS for the sub-Hilbert space of dimension N , the space is essentially a complete one. While performing the numerical calculation by using these two equations (eqn (36) and (37)), since we use the entire magnitude of NACTs, the validity of such equations clearly leads to the conclusion that the *ab initio* calculated NACTs do not have any non-removable component for the chosen sub-Hilbert space, N . Thereby, the calculated ADT matrix A will be theoretically “exact” and numerically “accurate” to calculate the diabatic PES matrix. In contrast, if it appears that those two equations are not numerically valid for a given sub-space of dimension N , one needs to expand the sub-Hilbert space to reach the desired level of accuracy, where the non-removable component becomes automatically zero and the removable component can be truly transformed to the diabatic one.

It is important to note that the solution of eqn (32) is independent of the product form of the rotation matrix constituted with different permutations as shown in eqn (34), which has been demonstrated elsewhere.⁸⁵ In contrast, such solution is dependent on the choice of contour over a two-dimensional (2D) nuclear CS due to the involvement of a skew-symmetric non-Abelian ($N \geq 3$) coupling matrix (τ). While solving eqn (32) along two different paths with the same initial and final nuclear coordinates (p_0, q_0 to $p_0 + \Delta p, q_0 + \Delta q$, see Fig. 3), we arrive at the following relation:³⁰

$$A_1^\dagger A_2 = A^\dagger(p_0, q_0) \exp(-\Delta p \Delta q (\text{curl}^{pq} \tau)) A(p_0, q_0), \quad (38)$$

where $\text{curl}^{pq} \tau = \left(\frac{\partial \tau_p}{\partial q} - \frac{\partial \tau_q}{\partial p} \right)_{(\bar{p}, \bar{q})}$, \bar{p} and \bar{q} are the midpoints of p_0 and $p_0 + \Delta p$, and q_0 and $q_0 + \Delta q$, respectively] represents the

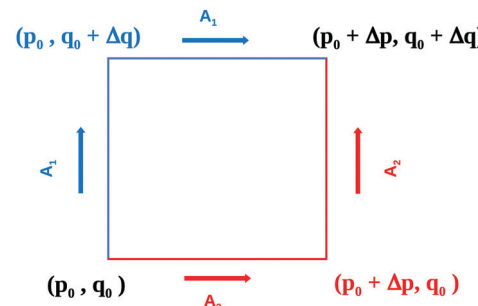


Fig. 3 The diagram depicts two different paths of integration for the ADT matrix (A) with the same initial (p_0, q_0) and final $(p_0 + \Delta p, q_0 + \Delta q)$ nuclear configurations, where the solutions (A_1 and A_2) are path dependent for non-Abelian situations.

magnitude of $\text{curl } \tau$ over the p - q nuclear plane. On the other hand, $A_1(p_0 + \Delta p, q_0 + \Delta q)$ and $A_2(p_0 + \Delta p, q_0 + \Delta q)$ are two solutions attended along two different contours at the end point (see Fig. 3). Hence, the two matrices are same only when $\text{curl}^{pq} \tau$ is zero, which is always true for two state sub-Hilbert space. On the other hand, the product matrix ($B = A_1^\dagger A_2$) shows the following property:

$$\begin{aligned} B^\dagger B &= A^\dagger(p_0, q_0) \exp(\Delta p \Delta q (\text{curl}^{pq} \tau)) A(p_0, q_0) A^\dagger(p_0, q_0) \\ &\quad \exp(-\Delta p \Delta q (\text{curl}^{pq} \tau)) A(p_0, q_0) = I \end{aligned} \quad (39)$$

even if $\text{curl}^{pq} \tau$ is non-zero for non-Abelian cases. The above relation implies that any two ADT matrices computed along two different contours are connected through an orthogonal transformation matrix (B), which ensures path-independence of the calculated observables³⁰ from the corresponding diabatic PESs.

It needs to be mentioned that this first principle based ADT methodology is equally applicable for molecules/processes with fewer atoms, like NO_2 ,^{76,77} H_3^+ ^{75,78,90} etc. to large molecules, namely, C_6H_6^+ ,^{80,104} $1,3,5\text{-C}_6\text{H}_3\text{F}_3^+$ ⁸³ or even more larger molecules. In other words, the ADT procedure can be implemented for chemical species of any number of electrons and nuclear DOFs. For three (3) nuclear DOFs, one has to carry out the procedure of contour integration on an infinite number of 2D cross sections of the original 3D space and such approach can be extended for systems with any higher number of DOFs to construct global diabatic PESs.^{84,85} Finally, it is important to highlight that the BBO theory *vis-à-vis* ADT procedure is equally applicable from higher symmetry group molecules (as for example $\text{NO}_2 \rightarrow C_{2v}$, $\text{NO}_3 \rightarrow D_{3h}$, $\text{C}_6\text{H}_6^+ \rightarrow D_{6h}$, etc.) to those molecules exhibiting no symmetry (C_1 symmetry). Nevertheless, during NACT calculation, the notion of point group has no meaning due to the consideration of non-rigidity of nuclear motion, where the MS group needs to be invoked to assign their IRREPs (see Subsection 4.2 for details).

In order to sketch the scheme of the ADT formalism for a realistic molecular species, we consider a nuclear CS by choosing two normal modes, bending (Q_1) and asymmetric stretching (Q_3) of NO_2 radical. In this prototype example, two low-lying electronic states (X^2A_1 and A^2B_2 at C_{2v} geometry and a pair of ${}^2\text{A}'$ states at C_s geometry) are nonadiabatically coupled through JT-type

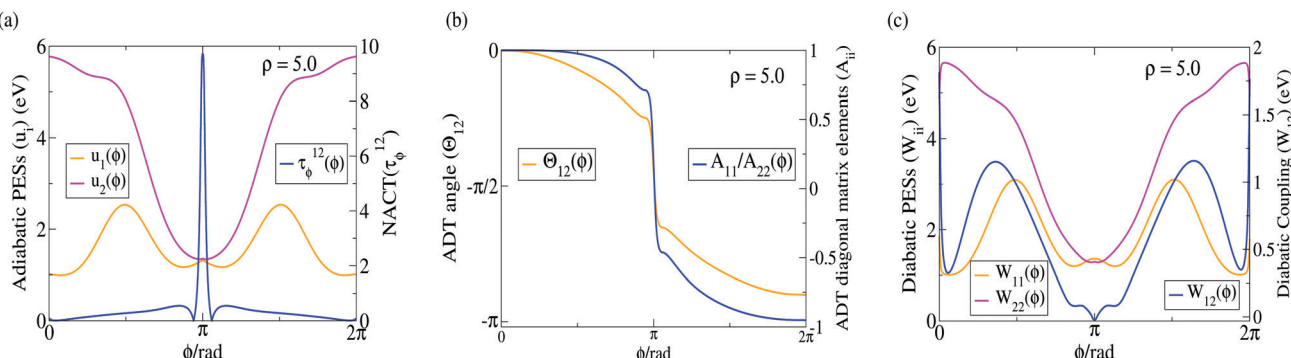


Fig. 4 For the NO_2 radical, two low-lying adiabatic PESs (X^2A_1 and A^2B_2) and the NACT between them are plotted along the ϕ coordinate for a fixed ρ value ($= 5.0$) in panel (a). Panel (b) depicts the ADT angle, Θ_{12} and the diagonal ADT matrix elements, $A_{11}[= A_{22}]$, which carry the signature of one JT CI by attaining close to π at $\phi = 2\pi$ and undergoing one sign inversion, respectively. Finally, panel (c) depicts smooth, single-valued and continuous functional characteristics of diabatic potential PESs (W_{11} and W_{22}) as well as coupling (W_{12}).

accidental CI seam and RT intersections, but they are decoupled from other excited states (B^2B_1 , $\text{C}^2\text{A}_2, \dots$) over the interested domain of nuclear CS.^{76,77} Hence, X^2A_1 and A^2B_2 can be considered as a two-state SHS and the corresponding adiabatic PESs are referred to as u_1 and u_2 , respectively. In order to construct a closed contour, the mass-weighted dimensionless normal mode coordinates (Q_1 and Q_3) are converted into their polar counterparts, ρ and ϕ ($Q_1 = \rho \cos \phi$ and $Q_3 = \rho \sin \phi$) and thereby, eqn (35) leads to the following two ADT equations:

$$\frac{\partial \Theta_{12}}{\partial \rho} = -\tau_\rho^{12}(\rho, \phi) \text{ and } \frac{\partial \Theta_{12}}{\partial \phi} = -\tau_\phi^{12}(\rho, \phi), \quad (40)$$

The NACT components (τ_ρ^{12} and τ_ϕ^{12}) are computed by *ab initio* quantum chemistry package MOLPRO¹⁰⁵ employing the MRCl level of methodology. Once the NACTs are in hand, the linear differential equations (eqn (40)) are integrated over the 2D contour by setting the initial magnitude of Θ_{12} as zero (0) at $\phi = 0$ and $\rho = 5.0$.

Fig. 4a depicts one-dimensional (1D) cuts of the lowest two adiabatic PESs (u_1 and u_2) as well as the angular component of NACT (τ_ϕ^{12}) along the ϕ coordinate for a fixed magnitude of ρ ($= 5.0$). The functional form of τ_ϕ^{12} shows a steep rise at $\phi = \pi$, where the JT CI seam intersects the contour. At the same ρ value, the resulting ADT angle [$\Theta_{12}(\rho, \phi)$] attains a magnitude close to π at $\phi = 2\pi$ and the diagonal elements of ADT matrices, $A_{11}[= A_{22}] = \cos \Theta_{12}(\rho, \phi)$ encounter single sign inversion bearing the signature of the '1–2' JT CI seam over the given nuclear CS (see Fig. 4b). Finally, the ADT matrices are employed to carry out the similarity transformation according to Eqn 33 for evaluating diabatic PESs and the couplings. Fig. 4c shows smooth functional variation of those quantities along the ϕ coordinate at the same ρ value.

4.2 Molecular symmetry adaptation of nonadiabatic coupling terms

While computing the adiabatic PESs with the electronic structure calculation, the BO approximation^{1,2} is invoked, where the nuclear configurations are kept freezed and thereby, one can assign the IRREPs of those PESs using point group symmetry.

On the contrary, NACTs are calculated as the derivative of nuclear coordinates over electronic states leading to non-Born–Oppenheimer situation of a molecular system and thereby, one needs to explore even higher symmetry groups to designate their IRREPs. The usability of the point group is limited for high amplitude nuclear (vibrational) motions of a species, where a larger set of symmetry operations is required to study the floppy molecular processes. If the time scale of a given laboratory experiment is shorter to permit certain nuclear permutations,¹⁰⁶ the MS group needs to consist of only the feasible ones among the elements of the complete group of Hamiltonians, which can be achieved without crossing an insurmountable energy barrier.

In general, an MS group of a molecule is composed of h symmetry operations, \hat{O}_i , $i = 1, 2, \dots, h$, namely, the identity operation E , all feasible permutations P of the spatial and spin coordinates of the equivalent nuclei, the inversion E^* of all nuclear (**R**) and electronic (**r**) coordinates, and the inversion-permutation $P \cdot E^*$ operation. One can express any such operation, \hat{O} as a product of three different operations,¹⁰⁷ i.e., $\hat{O} = \hat{O}_a \hat{O}_b \hat{O}_c$, where \hat{O}_a changes the vibronic DOFs, \hat{O}_b rotates the Euler angles, and \hat{O}_c permutes the nuclear spin. In contrast, only vibronic DOFs of a molecule are transformed by the symmetry operations of the point group.

We consider the example of a symmetric triatomic molecule, Na_3 cluster exhibiting D_{3h} symmetric equilibrium structure. The body fixed x - y - z axes are located in the cluster in such a manner that the plane of symmetry, σ_h passes through the molecular plane (xy plane) and the z axis coincides with the threefold symmetry axis, C_3 . Fig. 5 demonstrates those coordinate axes, symmetry elements and stereographic projection for the D_{3h} point group. In this case, the Cartesian coordinates x - y - z indicate the normal modes, Q_x (bending), Q_y (antisymmetric stretching) and Q_z (symmetric stretching), respectively. The atomic displacements for those vibrational modes are demonstrated in Fig. 6. In our study, we have chosen polar counterparts of x and y coordinates (ρ and ϕ) at a fixed magnitude of $z (= Q_z)$ at 3.7 Å. The following relations¹⁰⁷ can be established between the MS group [$D_{3h}(M)$] and the corresponding point group (D_{3h}):

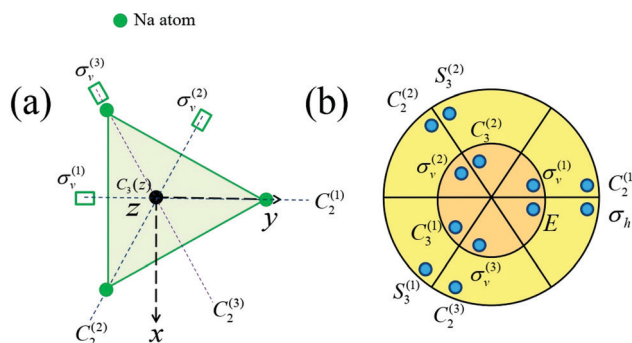


Fig. 5 The left diagram (a) describes symmetry elements of D_{3h} point group and the coordinate axes in a Na_3 system. The right one (b) shows the effects of those symmetry operations in the Na_3 cluster. The figure has been obtained from ref. 30.

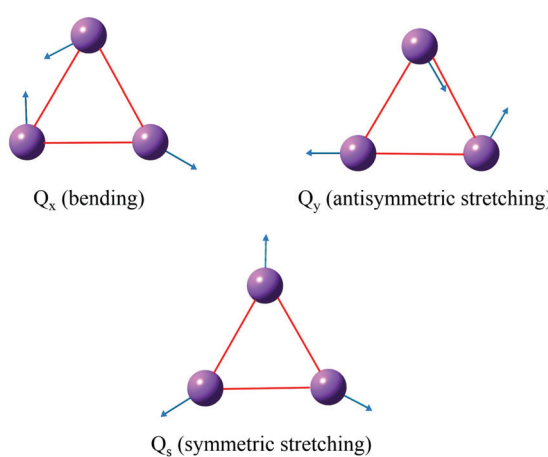


Fig. 6 The diagram shows vectorial displacements of the atoms in Na_3 cluster for three vibrational modes, namely Q_x (bending), Q_y (antisymmetric stretching) and Q_z (symmetric stretching).

$$E = E R^0 \cdot p_0, \quad (41a)$$

$$(123) = C_3^1 \cdot R^{\frac{2\pi}{3}} \cdot p_{123}, \quad (41b)$$

$$(23) = C_{2x} \cdot R^{\pi_z} \cdot p_{23}, \quad (41c)$$

$$E^* = \sigma_{xy} \cdot R^{\pi_z} \cdot p_0, \quad (41d)$$

$$(132)^* = S_3^{-1} \cdot R_z^{\frac{\pi}{3}} \cdot p_{132}, \quad (41e)$$

$$(23)^* = \sigma_{xz} \cdot R_y^{\pi} \cdot p_{23}, \quad (41f)$$

where “ R^ϕ ”s belong to the corresponding molecular rotation group and “ p ”s describe nuclear permutation. In order to define 1D IRREPs of NACTs for the $C_{2v}(M)$ group, Al-Jabour and his coworkers¹⁰⁸ proposed two important theorems, which have been extended for the corresponding $D_{3h}(M)$ group by Adhikari *et al.* for 2D IRREPs (see Section S6 of the ESI†).³⁰

Theorem 1: When the IRREP of a particular NACT along a specific symmetry adapted nuclear coordinate (R_l) is known, say $\tau_k^{\bar{j}}$, one can assign the IRREP of another one, $\tau_k^{\bar{i}}$ between the

same two electronic states i, j for a different symmetry adapted nuclear coordinate, R_k according to the following relation:

$$\begin{aligned} \Gamma(\tau_k^{\bar{j}}) &= \Gamma\left(\frac{\partial}{\partial R_k}\right) \times \Gamma\left(\frac{\partial}{\partial R_l}\right) \times \Gamma(\tau_l^{\bar{j}}) \quad \text{where} \\ \tau_k^{\bar{i}} &= \left\langle \xi_i \left| \frac{\partial}{\partial R_k} \right| \xi_j \right\rangle_r \end{aligned} \quad (42)$$

It is important to note that the theorem is valid only for those nuclear coordinates that belong to 1D IRREP of the MS group. Since one of the IRREPs has to be fixed arbitrarily, we can find different combinations of those IRREPs using eqn (42).

For the Na_3 cluster (D_{3h} system), we have implemented the above theorem to obtain the possible sets of IRREPs for the NACTs (τ_ρ , τ_ϕ , τ_x and τ_y) and then, applied the quantization rule to find out the physically realizable one: $\oint dR \cdot \tau = \pm n\pi$, which implies $\tau_\phi \in A'_1$, $\tau_\rho \in A''_1$ and $\tau_x, \tau_y \in E'$.³⁰ Section S6 of the ESI† provides an extensive analysis of the first theorem on Na_3 , where Table S5 (ESI†) demonstrates the extended character table for the MS group $D_{3h}(M)$.

Theorem 2: The IRREP of NACT along a definite symmetry-adapted nuclear coordinate is related to the IRREPs of other NACTs for the same nuclear coordinate among different electronic states.

In order to validate the above statement, a loop-type sequence of N molecular states of same spin multiplicity, namely N doublet states, $D_a, D_b, D_c, \dots, D_y, D_{z=a}$ is considered and the product NACT becomes:

$$\tau_k^{a,b,c,\dots,y,z=a} = \tau_k^{a,b} \tau_k^{b,c} \dots \tau_k^{y,z=a}. \quad (43)$$

For 1D IRREP,¹⁰⁸ employing eqn (43), one can write the following relation:

$$\begin{aligned} \Gamma\left(\tau_k^{a,b,c,\dots,y,z=a}\right) &= \Gamma(\xi_a)^2 \times \Gamma(\xi_b)^2 \times \dots \times \Gamma(\xi_y)^2 \times \Gamma\left(\frac{\partial}{\partial R_k}\right)^N \\ &= \begin{cases} \Gamma\left(\frac{\partial}{\partial R_k}\right) & \text{when } N \text{ is odd} \\ A'_1 & \text{when } N \text{ is even} \end{cases} \end{aligned} \quad (44)$$

We have extended³⁰ Theorem 2 to designate 2D IRREPs for corresponding $D_{3h}(M)$ group employing a prototype example, Na cluster, where the following relationship holds:

$$\Gamma(\tau_k^{1,2,3,1}) = \Gamma(\tau_k^{12}) \times \Gamma(\tau_k^{23}) \times \Gamma(\tau_k^{31}) = \Gamma(\tau_k^{12}) \times \Gamma(\tau_k^{23})^2 \quad (45)$$

imposing the conditions, $\Gamma(\tau_k^{31}) = \Gamma(\tau_k^{13})$ and $\Gamma(\tau_k^{13}) = \Gamma(\tau_k^{23})$ as per the crossing rule (depicted in Section S6 of the ESI†):

$$\Gamma(\tau_k^{i,j}) = \Gamma(\tau_k^{(i+1),j}), \quad (46)$$

if a CI is present between the i th and $i + 1$ th electronic states. According to 2D IRREPs of $D_{3h}(M)$ symmetry, $\Gamma(\tau_k^{23})$ leads to the following relation,

$$\begin{aligned} \Gamma(\tau_k^{23}) &= \Gamma(\xi_2) \times \Gamma\left(\frac{\partial}{\partial x}\right) \times \Gamma(\xi_3) \\ &\Rightarrow E' = \Gamma(\xi_2) \times E' \times \Gamma(\xi_3) \\ &\Rightarrow \Gamma(\xi_2) \times \Gamma(\xi_3) = A'_1 \end{aligned} \quad (47)$$

In a similar way, for $\Gamma(\tau_x^{13})$,

$$\Gamma(\xi_1) \times \Gamma(\xi_3) = A'_1. \quad (48)$$

Since the above relations clearly demonstrate that ξ_1 , ξ_2 and ξ_3 belong to 1D IRREP (A'_1), we arrive at the following relationship by exploiting the second theorem (eqn (44)):

$$\begin{aligned} \Gamma(\tau_x^{1,2,3,1}) &= \Gamma(\xi_1)^2 \times \Gamma(\xi_2)^2 \times \Gamma(\xi_3)^2 \times \Gamma\left(\frac{\partial}{\partial x}\right)^3 \\ &= A'_1 \times \Gamma\left(\frac{\partial}{\partial x}\right)^3 = \Gamma\left(\frac{\partial}{\partial x}\right)^3 = (E')^3 \end{aligned} \quad (49)$$

On the other hand, from eqn (45), we get,

$$\begin{aligned} \Gamma(\tau_x^{1,2,3,1}) &= \Gamma(\tau_x^{12}) \times \Gamma(\tau_x^{23})^2 \\ &= \Gamma(\tau_x^{12}) \times (E')^2 \end{aligned} \quad (50)$$

and then, by comparing eqn (49) and (50), one can find $\Gamma(\tau_x^{12}) = E'$. In a similar way, we can assign the IRREPs for the y components of NACTs.

In Section S6 of the ESI,[†] both of the above theorems are elaborately discussed for 2D IRREPs and the extended character table for the $D_{3h}(M)$ group is presented.

5 Extended Born–Oppenheimer equations

In order to incorporate the nonadiabatic effects originating from other electronic states to a specific one as an effective vector potential, one needs to formulate single surface extended Born–Oppenheimer (EBO) equations, which is an intermediate representation between adiabatic and diabatic ones.^{5,6,12,71,86,87,109–113} While developing EBO equations, the BO equations are modified by bringing the contribution of off-diagonal elements of NACM in the diagonals of the Hamiltonian matrix and then, the classical inaccessibility condition for a specific state from others is imposed assuming the occurrence of the molecular process within a narrow energy width. Baer and Englman^{109,110} took the first successful attempts to formulate a set of approximated EBO equations for a two-state SHS by incorporating the effect of nonadiabatic couplings on each single surface. Those equations were employed to compute transition probabilities in a two-arrangement channel model, which are in good accord with the results evaluated from diabatic PESs.^{5,12} In an alternate approach, Varandas and Xu⁶ arrived at the EBO equations for two state electronic manifold in terms of mixing angles. Later on, the EBO formalism for three coupled electronic states was developed by Baer *et al.*^{111,112} taking an arbitrary form of the τ matrix with constant elements. After a few years, Adhikari and his coworkers generalised the BO treatment^{71,86,87,113} from first principle for three and higher dimensional sub-space employing the explicit forms of NACTs and derived the EBO equations as functions of ADT angles.^{71,86,113}

While developing single surface EBO equation for a set of coupled electronic states, it is necessary to embed the effect of off-diagonal elements of τ into the diagonal. Such a concept can

be executed if NACM can be factorized into a vector function and a skew-symmetric scalar matrix. This product form is possible only when two different scalar components of NACM commute with each other (*i.e.* $\text{curl } \tau = 0$) over the entire nuclear CS, which is always true for Abelian case ($N = 2$). On the other hand, the scalar components of NACM generally do not commute for the non-Abelian ($N \geq 3$) situations (*i.e.* $\text{curl } \tau \neq 0$), but at the close neighbourhood of a degenerate point, the curl can be approximated to zero ($\text{curl } \tau \approx 0$).^{71,86,87,113} Such a situation can be realized by considering the parametric representation for the vector equation of a conical surface at the degenerate point, where the determinant (Jacobian) for transformation from Cartesian to polar coordinates or *vice versa* turns to zero (0). Indeed, it is necessary to fulfil the gauge invariance (GI) condition by the angular component of the eigenvalues of NACM (ω_ϕ) over the domain of nuclear CS. In our recent works, the possibility of formulating single-surface EBO equations has been explored for NO_3 and TFBz^+ ⁸⁷ by computing curl equations ($\text{curl } \tau$) and GI of the eigenvalues (ω_ϕ) at and around a CI point.

Once the factorization of NACM into a vector function and a scalar matrix is accomplished, the adiabatic SE (eqn (29)) can be converted into an intermediate representation by employing a unitary transformation matrix G , which diagonalizes the skew-symmetric vector matrix, τ and the transformed SE is represented as:

$$-\frac{\hbar^2}{2}(\nabla_R G + \Omega)^2 \Phi + (V - E)\Phi = 0, \quad (51)$$

where $\psi^{\text{ad}} = G\Phi$, $\Omega = G^\dagger \tau G = i\omega$ and $V = G^\dagger U G$.

The approximations involved in the process of evaluating the expression of ω are valid if its angular component satisfies the following GI condition:

$$\int_0^{2\pi} \omega_\phi d\phi = n\pi, \quad (52)$$

where n indicates the number of CI(s)/seam(s) encapsulated within the closed loop of integration. Assuming the G matrix elements as slowly varying functions of nuclear coordinates, it is observed that G commutes with ∇_R and hence, eqn (51) can be simplified as,

$$-\frac{\hbar^2}{2}(\nabla_R + \Omega)^2 \Phi + (V - E)\Phi = 0, \quad (53)$$

In the above expression, V is a full matrix, which is given as:

$$(V\Phi)_i = u_i \Phi_i + \sum_{j \neq i}^N G_{ij}^*(u_j - u_i) \psi_j^{\text{ad}}, \quad i = 1, 2, 3, \dots, N \quad (54)$$

It is necessary to note that the first term indicates the product of the adiabatic energy (u_i) with the wavefunction (Φ_i) for the i th electronic state, while the contribution of the remaining summation is negligible ($|\psi_i^{\text{ad}}| \gg |\psi_j^{\text{ad}}|$) due to the classical forbidden condition beyond the width of a specific energy. Moreover, the summation turns into zero at the degenerate points, as $u_1 = u_2$ and $u_1 = u_2 = u_3$ for a two and three state degeneracy, respectively. In any case, eqn (53) is simplified to formulate the following set of single-surface

EBO equations:

$$-\frac{\hbar^2}{2}(\nabla_R + \Omega_{ii})^2\Phi_i + (u_i - E)\Phi_i = 0, \quad i = 1, 2, 3, \dots, N. \quad (55)$$

In summary, one can employ such formalism to decouple ' N ' number of coupled SEs to ' N ' independent EBO equations by incorporating the effects of other electronic states on a specific one. Section S7 of the ESI† describes an extensive theoretical formulation of EBO equations for the Abelian case ($N=2$) as well as one non-Abelian case ($N=3$).

While formulating EBO equations for non-Abelian situations, it is required to verify two conditions, namely, $\text{curl } \tau \simeq 0$ vis-à-vis the GI of the eigenvalues (ω_ϕ) at the close vicinity of the CI(s) and the classical inaccessibility of an electronic state from the other states at a specific energy. We demonstrate the validity of GI of NACM eigenvalues numerically for three realistic molecular systems (NO_2 radical, NO_3 radical and a triatomic reactive system, $\text{F} + \text{H}_2$)⁸⁷ over the interested domain of nuclear CS around the CI point(s).

In order to explore the validity of the GI condition for NO_2 and NO_3 molecules, we have taken nuclear planes by considering the polar counterparts, $\rho\phi$ of $Q_1\text{-}Q_3$ (bending and asymmetric stretching) and $Q_{3x}\text{-}Q_{3y}$ (degenerate asymmetric stretching) normal modes, respectively. On the other hand, for triatomic reactive system, $\text{F} + \text{H}_2$, the eigenvalues (ω_ϕ) and their GIs have been calculated along a closed circular path as demonstrated in Fig. 7a and b. Fig. 8(a–e) describe 1D variation of one of the non-zero eigenvalues (ω_ϕ) and their GIs ($\int_0^{2\pi} \omega_\phi d\phi$) along a circular contour for NO_2 , $\text{F} + \text{H}_2$ and NO_3 . In the case of NO_2 radical, the closed loop at $\rho = 10.6$ encompasses a semicircular JT type seam (C_s symmetric seam passing through a C_{2v} point) and RT interactions within the low-lying $X^2\text{A}_1$ and $A^2\text{B}_2$ states, which is reflected (Fig. 8a) in the magnitude of corresponding GI ($\int_0^{2\pi} \omega_\phi d\phi \simeq 3\pi$). On the other hand, the quantity, $\int_0^{2\pi} \omega_\phi d\phi$ for $\text{F} + \text{H}_2$ at specific values of q , r_{HH}

and R_{ce} [see Fig. 7a and b] reaches close to π and 2π at the end of the contour due to the presence of one JT [$1^2\text{A}'$ and $2^2\text{A}'$ ('1–2')] CI and one RT [$2^2\text{A}'$ and $1^2\text{A}''$ ('2–3')] intersection, respectively (see Fig. 8b and c). Finally, in the case of NO_3 , JT type CIs are present within $\tilde{\text{A}}^2\text{E}''$ ('2–3') and $\tilde{\text{B}}^2\text{E}'$ ('4–5') states encircled by the contour at $\rho = 0.4$ and $\rho = 3.5$, respectively, and the integration of the corresponding eigenvalues along these paths acquires a magnitude close to π and 4π fulfilling the GI condition approximately (see Fig. 8d and e).

Although it is possible to decouple the electronic states through the EBO approach, the main shortcoming of formulating the single surface equations lies in the choice of nuclear CS. The validity of approximation of $\text{curl } \tau \simeq 0$ is ensured only at the close vicinity of a CI point. Hence, we can formulate the EBO equations and achieve converged numerical results only over a specific domain of nuclear CS.

6 BBO theory vis-à-vis contemporary approaches

The theoretically “exact” first principle based BBO theory is highly useful to construct numerically “accurate” diabatic PESs and couplings employing *ab initio* adiabatic surfaces and NACTs for spectroscopic systems as well as scattering processes.⁸⁴ This implies that our approach is equally applicable around the Franck–Condon (FC) domain and also at the asymptotic region of nuclear CS. In this section, the key features of the BBO theory are briefly demonstrated in comparison with other contemporary methodologies, which also attempt to incorporate the contribution of ground as well as coupled excited states in a molecular/chemical process.

6.1 Aspects of contemporary methodologies

(a) Vibronic coupling model: according to the vibronic coupling model (VCM),⁴⁵ the diagonal and off-diagonal diabatic matrix elements are assumed to show up linear, bilinear or even higher order functional dependence of nuclear DOFs with respect to the ground adiabatic PES ($V_0(\mathbf{R})$) minima or more preferably, the CI point (\mathbf{R}_0).^{46–48,53,56} Recently, Zeng *et al.*^{57,58} took an attempt to formulate general expressions of diabatic Hamiltonian up to arbitrary order for trigonal and tetragonal systems. For the sake of simplicity, if linear VCM is considered those diabatic matrix elements are expanded in a Taylor series at the vicinity of a reference nuclear geometry, \mathbf{R}_0 as:

$$\begin{aligned} W_{ii}(\mathbf{R}) &= \hat{T}_{\text{nuc}} + V_0(\mathbf{R}) + W_{ii}(\mathbf{R}_0) + \sum_s \kappa_s^{(i)} R_s \\ W_{ij}(\mathbf{R}) &= \sum_s \lambda_s^{(i,j)} R_s \quad i \neq j, \end{aligned} \quad (56)$$

where $W_{ii}(\mathbf{R})$, $W_{ij}(\mathbf{R})$ represent diabatic potential energy matrix elements, and the combining coefficients ($\kappa_s^{(i)}$ and $\lambda_s^{(i,j)}$) symbolize linear vibronic coupling constants. It is worthwhile to mention that the validity of the above model is ensured only in a limited domain of FC region at the close neighbourhood of reference geometry \mathbf{R}_0 , where the ground state should be nondegenerate with the excited ones.

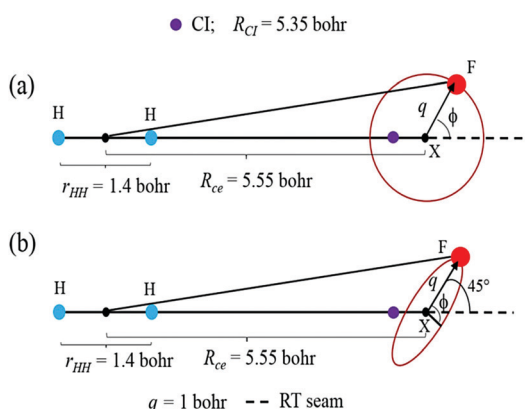


Fig. 7 The diagrams depict the contour of radius, $q = 1.0$ bohr traversed by the F atom around the center, X, which is placed on the collinear H_2 axis. In this arrangement, r_{HH} (H–H distance), R_{ce} (distance from the center of closed contour, X to the center of mass of H–H) and R_{CI} (distance from the CI to the center of mass of H–H) are considered as 1.401 bohr, 5.55 bohr and 5.35 bohr, respectively. In upper panel (a), the contour is in plane with the H–H–X axis, whereas in the lower one (b), the loop is tilted by 45° with respect to the same axis.

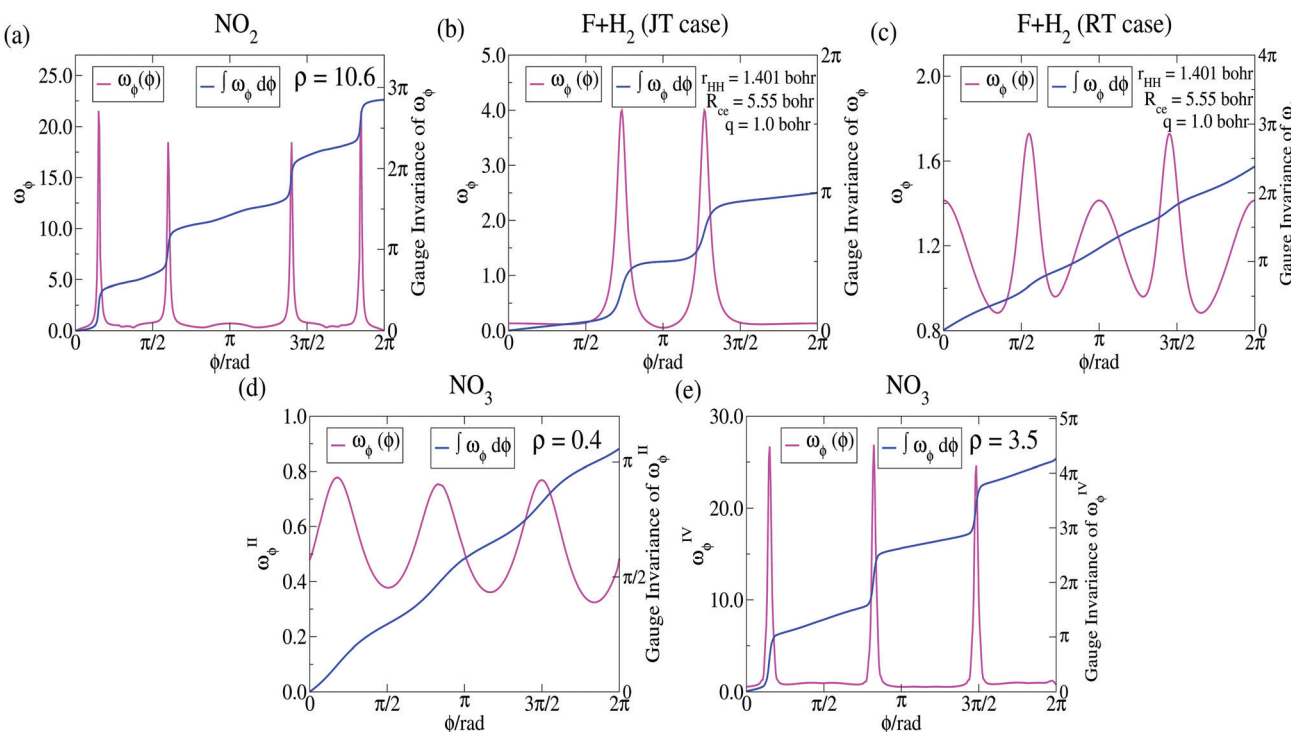


Fig. 8 Eigenvalues of NACM and their gauge invariance (GI) are plotted as function of ϕ coordinate for NO_2 radicals at $\rho = 10.6$ in panel (a). Panel (b) and (c) depict 1D variation of ω_ϕ s and their GIs for the $\text{F} + \text{H}_2$ system at $q = 1.0$ bohr, with $r_{\text{HH}} = 1.401$ bohr and $R_{\text{ce}} = 5.55$ bohr for '1–2' JT and '2–3' RT interactions, respectively. Diagrams (d) and (e) represent the same quantities (ω_ϕ s and their GIs) for the NO_3 radical at $\rho = 0.4$ for '2–3' CI (JT) and $\rho = 3.5$ for '4–5' CIs (JT and three accidental), respectively.

(b) Exact factorisation method: Gross *et al.*^{59–61} introduced the exact factorization (EF) scheme in which the electronic and nuclear SEs are numerically solved concurrently employing the time-dependent PESs, vector potential and a coupling operator. In this approach, the wavefunctions cannot designate a specific quantum state and thereby, the physical significance of such functions is not clear with respect to the adiabatic states and the correlations within them. This method has been implemented to investigate the contribution of CI(s) on dynamical calculations for 2D model systems^{114,115} as well as realistic species, where the electronic structure calculations have been carried out by a TDDFT based approach.¹¹⁶

(c) Direct dynamics: several direct-dynamics (DD) methods, namely, on-the-fly diabatization version of multi-configurational time-dependent Hartree (MCTDH)^{62,63} and DD variational multi-configurational Gaussian (DD-vMCG)^{64–66} approaches have been developed to perform nonadiabatic dynamics. In these methodologies, ADT matrix, $A(\mathbf{R})$ is evaluated by taking line integrals of the NACT between any two adiabatic states at the close neighbourhood of a CI point/seam, *i.e.*, the following expression is numerically integrated at every step of time propagation.⁶⁵

$$\nabla_R A(\mathbf{R}) = -\tau(\mathbf{R})A(\mathbf{R}) \quad (57)$$

for which the solution is given by:^{39,117}

$$A(\mathbf{R} + \Delta\mathbf{R}) = \exp\left(-\int_{\mathbf{R}}^{\mathbf{R} + \Delta\mathbf{R}} \tau \cdot d\mathbf{R}\right) A(\mathbf{R})$$

It is noteworthy to highlight that one can employ our BBO approach to find out a more formal solution of eqn (57) using eqn (35), which incorporates all the electronic states constituting the SHS instead of two states forming the CI point/seam.

6.2 Features of BBO theory: possibilities and challenges

(a) While carrying out BBO theory based diabatization, the BO expansion of the total molecular wavefunction takes the following form,

$$\begin{aligned} \Psi(\mathbf{r}, \mathbf{R}) &= \sum_i \psi_i^{\text{ad}}(\mathbf{R}) \xi_i(\mathbf{r}; \mathbf{R}) = \sum_i \psi_i^{\text{ad}}(\mathbf{R}) A(\mathbf{R}) \tilde{\xi}_i(\mathbf{r}) \\ &= \sum_i \psi_i^{\text{dia}}(\mathbf{R}) \tilde{\xi}_i(\mathbf{r}), \end{aligned}$$

where $\tilde{\xi}_i(\mathbf{r})$ s no longer depend on nuclear coordinates (\mathbf{R}) and consequently, the derivatives of $\tilde{\xi}_i(\mathbf{r})$ s with respect to those coordinates (\mathbf{R}) vanish. The "exact" form of $A(\mathbf{R})$ matrix can be evaluated by employing eqn (32) (more explicitly, eqn (35)) and then, it is plugged into eqn (33) to calculate the diabatic PES matrix at each nuclear configuration, \mathbf{R} . In the quasi-diabatic VCM method (depicted in Subsection 6.1), the diabatic potential matrix elements ($W_{ij}(\mathbf{R})$) are expressed in terms of Taylor series expansion around the ground state minima or a CI point (\mathbf{R}_0) including linear, bilinear or even higher order terms. In contrast, our BBO approach can accurately describe the diabatic PESs and the coupling terms up to all order even for the accidental CIs for spectroscopic systems. Moreover, such

approach is employed to construct global diabatic PESs for scattering processes, where diabatization is required even in the asymptotic region of nuclear CS.

(b) While performing the diabatization based on BBO theory even with MRCI level “accurate” adiabatic PESs and NACTs, it appears for one of the components in most of the degenerate pairs of asymmetric stretching/bending modes or even for specific non-degenerate asymmetric stretching modes that the diabatic coupling elements along those modes produce symmetric functional form (even-parity). We have seen that the matrix element of those potential coupling terms is only fitted with even power polynomial over and above the harmonic potential for such modes on the diagonal. For each pair of modes involving those specific asymmetric stretching/bending vibrations, the general form of potential energy matrix element (lets say, one of the off-diagonal elements) can be written as:

$$W_{ij}(Q_x, Q_y) = \sum_{n=0}^N \sum_{m=0}^M c_{nm} Q_x^n Q_y^{2m} \quad n, m \in \{0, 1, 2, \dots\}$$

where i, j are two electronic states and Q_x, Q_y are two normal modes. Such a fitted polynomial clearly depicts that there will be no contributing coefficients ($c_{01}, c_{11}, c_{21}, \dots$), namely, for $Q_y, Q_x Q_y, Q_x^2 Q_y, \dots$ at least up to the numerical precision. We find that there are several degenerate asymmetric stretching/bending as well as non-degenerate stretching modes in various molecular systems,^{30,77,83–85,88} where some of those coupling elements are presented in Fig. S9 (1D cut) and Fig. S10 (2D contour) of the ESI.† The reason behind the symmetric functional form of diabatic PESs and couplings along the asymmetric mode(s) is originating due to the symmetric nature of adiabatic PESs and NACTs (as for example see Fig. S11 of the ESI† for a Q_{3x} normal mode of NO_3) along the same mode(s), which are obtained by the state-of-the-art accurate *ab initio* calculations.

In traditional JT models, appropriate symmetry on the functional forms of diabatic PES matrix elements has been incorporated^{53,55,56} so that the diabatic Hamiltonian turns into totally symmetric (A). On the other hand, we employ MS adaptation to assign appropriate IRREPs of the *ab initio* calculated NACTs to carry out the diabatization, which leads to a totally symmetric diabatic PES matrix [see Subsection 4.2 (Molecular symmetry adaptation of nonadiabatic coupling terms)]. Even then, certain asymmetric stretching modes show up even-parity in their functional forms both for adiabatic PESs as well as NACTs. After adiabatic-to-diabatic transformation (ADT), the diabatic matrix elements depict even-parity and thereby, those coupling terms are fitted only with even power polynomials.

(c) In BBO treatment, the presence of JT CI(s)/seam(s) (symmetry allowed or accidental) or RT interaction(s) can be verified by the quantized nature of ADT angle(s), which acquire the numerical value of $n\pi$ (n is an integer) at the end of closing the contour. Such property enables us to ensure the nature and accuracy of the diabatic PES matrices. Nevertheless, such analogous procedure is unavailable in the quasi-diabatization method to verify the accuracy of diabatic PESs.

(d). Recently, we have developed an efficient generalized algorithm and program, ‘ADT’⁸⁵ (see <https://pubs.acs.org/doi/10.1021/acs.jctc.9b00948> or <https://github.com/AdhikariLAB/ADT-Program>)

to generate analytic expressions of several ADT quantities (ADT equations, diabatic potential energy matrix, etc.) as well as to calculate those quantities numerically (eqn (33)–(35)) for any N number of coupled electronic states with M nuclear coordinates. While carrying out numerical calculations, the *ab initio* data (adiabatic PESs and NACTs) can be directly provided as input files to this software or those files can be generated through in-built python codes interfacing standard quantum chemistry packages, like MOLPRO,¹⁰⁵ Gamess¹¹⁸ and Gaussian.¹¹⁹ Nevertheless, computation of good quality *ab initio* inputs, namely, adiabatic PESs and NACTs is really a challenging issue for extensive use of our first principle based diabatization. In future, our ‘ADT’ algorithm is expected to make required changes to interface with direct dynamics (DD) approaches as mentioned in Subsection 6.1 to generate diabatic curves or surfaces.

7 Applications of the Jahn–Teller model in rare earth manganites LaMnO_3

The higher energy satellite transitions accompanied with inter-site ($d^4 d^4 \rightarrow d^3 d^5$) 1.96 eV optical electronic excitation^{21–24,120} appear at 2.29 ± 0.02 eV, 2.41 ± 0.02 eV, 2.66 ± 0.02 eV and 2.84 ± 0.02 eV in the room-temperature a -axis (in $Pbnm$ symmetry) optical ellipsometry spectra.^{21–24} The anomalous temperature dependent behaviors^{21–24} of such peak energies (shift down by 80, 20, and 110 meV) and widths below Néel temperature ($T_N \simeq 140$ K) indicate their roto-vibrational origin associated with the pseudo-rotational levels of both lower and upper branches of ‘Mexican hat’ APES.

Taking into account the theoretically calculated average energies for doublet sets of roto-vibrational levels [17/2–19/2 (0.253 eV)], [23/2–25/2 (0.448 eV)], [29/2–31/2 (0.699 eV)] and [35/2–37/2 (1.006 eV)] of a ground electronic state at static limit ($\beta = 375 \text{ cm}^{-1}$)²⁰ as well as by including the optical electronic transition shift (1.96 eV), a good accordance between theory²⁰ and experiment^{21–24} is observed for (ii) 2.41 ± 0.02 eV and (iii) 2.66 ± 0.02 eV excitations. However, theoretically calculated peaks at (i) 2.21 eV and (iv) 2.97 eV²⁰ are away from the respective experimental transitions, 2.29 ± 0.02 eV and 2.84 ± 0.02 eV (see Table 1). It is worth mentioning here that theoretical calculations have been carried out by considering a model²⁰ to study the JT effect in a cubic symmetry,^{15,17} which consists of only one single octahedral unit.¹⁹

In contrast, theoretically calculated peaks²⁰ (i) 2.29 eV and (iii) 2.63 eV considering doublet sets of cubic perturbed centrifugally stabilized excited electronic state, pseudo-rotational levels (i) $\pm 1/2, \pm 3/2$; 0.327 eV and (iii) $\pm 9/2, \pm 11/2$; 0.672 eV display excellent concurrence with the experimental transitions,^{21–24} 2.29 ± 0.02 eV, and 2.66 ± 0.02 eV, respectively. On the other hand, the theoretically obtained satellite peaks at 2.47 and 2.78 eV resulting from average eigenvalues of roto-vibrational levels (ii) $\pm 5/2, \pm 7/2$; 0.511 eV and (iv) $\pm 13/2, \pm 15/2$; 0.817 eV²⁰ are slightly distant from the corresponding experimental peaks at 2.41 ± 0.02 and 2.84 ± 0.02 eV^{21–24} (see Table 2).

Table 1 Comparative study between theoretical and experimental peak positions (ν_{Exp}) assigned from the pseudo-rotational levels of the cubic perturbed low-energy sheet of the 'Mexican Hat' APES of LaMnO₃ complex, where $\alpha = 25 \text{ cm}^{-1}$, $\beta = 375 \text{ cm}^{-120,121-123}$ and the shift due to optical electronic transition is equal to 1.96 eV^{21-24,120} (the table is taken from ref. 20)

Roto-vibrational level ($\pm l$)	$\varepsilon + \beta [\text{cm}^{-1}]$ ($\beta = 375 \text{ cm}^{-1}$)	$\varepsilon_{\text{average}}$ (eV)	Shift + $\varepsilon_{\text{average}}$ (eV)	ν_{Exp} (eV)
$\pm 17/2$	2194.34	0.253	2.21	2.29 ± 0.02
$\pm 19/2$	2639.26			
$\pm 23/2$	3686.66	0.448	2.41	2.41 ± 0.02
$\pm 25/2$	4285.82			
$\pm 29/2$	5634.67	0.699	2.66	2.66 ± 0.02
$\pm 31/2$	6384.24			
$\pm 35/2$	8045.86	1.006	2.97	2.84 ± 0.02
$\pm 37/2$	8945.00			

Table 2 Comparative study between theoretical and experimental peak positions (ν_{Exp}) assigned from the pseudo-rotational levels of cubic perturbed centrifugally stabilized upper sheet of the 'Mexican Hat' APES of the LaMnO₃ complex, where the shift of optical electronic transition is equal to 1.96 eV^{21-24,120} (the table is borrowed from ref. 20)

Roto-vibrational level ($\pm l$)	$\bar{E}_{s=0,\pm l}^{\text{cp+b,vib}}$ [cm ⁻¹]	$\langle \bar{E}_{s=0,\pm l;\pm l+1}^{\text{cp+b,vib}} \rangle$ (eV)	Shift + $\langle \bar{E}_{s=0,\pm l;\pm l+1}^{\text{cp+b,vib}} \rangle$ (eV)	ν_{Exp} (eV)
$\pm 1/2$	2254.09	0.327	2.29	2.29 ± 0.02
$\pm 3/2$	3021.01			
$\pm 5/2$	3774.73	0.511	2.47	2.41 ± 0.02
$\pm 7/2$	4469.21			
$\pm 9/2$	5116.46	0.672	2.63	2.66 ± 0.02
$\pm 11/2$	5729.75			
$\pm 13/2$	6312.56	0.817	2.78	2.84 ± 0.02
$\pm 15/2$	6871.97			

Our theoretical investigations²⁰ account the effect of anharmonicity on the excited JT state very accurately for the first time. Moreover, such model²⁰ reveals the crucial contribution of lower roto-vibrational levels of the centrifugally stabilized excited state to the dielectric function of LaMnO₃ in the 2.2–2.9 eV spectral range²¹⁻²⁴ (showing anomalous temperature dependent trend at around $T_N \simeq 140 \text{ K}^{21-24}$) compared to very high pseudo-rotational levels²⁰⁻²⁴ associated with the anharmonic ground electronic state.

8 Construction of the diabatic Hamiltonian and nuclear dynamics for spectroscopic processes

In this section, we review the workability of first principle based BBO theory to explore various types of nonadiabatic interactions and their role in the photodetachment spectra of some prototype molecular species at and around the FC region of nuclear CS. Subsection 8.1 depicts the construction of highly accurate diabatic PESs for the low-lying two electronic states of the NO₂ radical (X²A₁ and A²B₂)^{76,77} and presents theoretically computed photoelectron spectra of the NO₂⁻ anion in comparison with the experimentally measured one.⁹⁴ On the other hand, Subsection 8.2 demonstrates theoretical spectra of the Na₃ cluster, which are calculated by employing both the model diabatic Hamiltonian

matrix introduced by Cocchini *et al.*^{124,125} as well as the BBO theory based diabatic PES matrix³⁰ for three excited states (2²E' and 1²A'). Subsection 8.3 is dedicated to analyse the non-adiabatic couplings present within five electronic states for the molecular species, namely, NO₃ radical ($\tilde{X}^2\text{A}'_2$, $\tilde{\text{A}}^2\text{E}''$ and $\tilde{\text{B}}^2\text{E}'$)⁸⁰⁻⁸² and Bz⁺ radical cation ($\tilde{X}^2\text{E}_{1g}$, $\tilde{\text{B}}^2\text{E}_{2g}$ and $\tilde{\text{C}}^2\text{A}_{2u}$).^{80,104} This section also presents theoretical photodetachment spectra of the NO₃⁻ anion obtained from BBO based diabatic PESs, which shows excellent agreement with the experimental finding.⁹⁶ Finally, the implementation of six state BBO theory on the TFBz⁺ radical cation ($\tilde{X}^2\text{E}''$, $\tilde{\text{A}}^2\text{A}''_2$, $\tilde{\text{B}}^2\text{E}'$ and $\tilde{\text{C}}^2\text{A}'_2$)⁸³ is summarized in Subsection 8.4. The diabatic PESs of the aromatic radical cations, Bz⁺ and TFBz⁺ will be employed to carry out dynamical calculations in the near future.

8.1 Molecular system with two coupled electronic states: NO₂

Nitrogen dioxide (NO₂) radical shows JT and RT interactions within its lowest two electronic states (X²A₁ and A²B₂), which play a key role in assigning its theoretical photoelectron spectrum^{49,76,77,126-133} in comparison with the experimental one.⁹⁴ Our group has constructed highly precise diabatic surfaces of NO₂⁷⁷ employing MRCI based adiabatic PESs and NACT obtained from the MOLPRO¹⁰⁵ quantum chemistry package. Finally, nuclear dynamics has been carried out to reproduce the experimental photoelectron spectra of its anionic analogue, NO₂⁻.⁷⁷

In the NO₂ molecule, JT type symmetry allowed accidental conical intersections (SAACIs) and RT interactions are explored over three 2D nuclear planes (Q_i-Q_j) consisting of bending (Q_1), symmetric (Q_2) and asymmetric stretching (Q_3) normal modes. The ρ component of NACT (τ_{ρ}^{12}) over the polar plane ($\rho-\phi$) corresponding to Q_1 and Q_3 is presented in Fig. 9a, which clearly indicates the existence of one JT type seam passing through the C_{2v} point with three peaks [one at C_{2v} (peak 1) and the other two at C_s (peaks 2 and 3) nuclear geometries], whereas the RT intersections are prominent at the linear nuclear CS (peaks 4 and 5).^{76,77} While carrying out the first principle based ADT procedure along a closed contour at $\rho = 10.7$, Fig. 9b depicts the resulting ADT angle (Θ_{12}), which acquires the magnitude of 3π bearing the signature of JT type CI seam (π) and RT interaction (2π).^{77,85} In two other pairs, namely, Q_1-Q_2 and Q_2-Q_3 , two JT SAACIs and one RT intersection are observed for each case over the 2D nuclear planes, which is evident from the singularities of the NACT landscapes.⁷⁷ Finally, the ADT matrix is used to construct a two-state three-mode diabatic Hamiltonian, where PESs and coupling elements are smooth, single-valued and continuous over the interested domain of nuclear CS. Moreover, it is worthwhile to mention that along the Q_3 normal mode, the diabatic coupling element exhibits symmetric and nonlinear functional characteristics (see Fig. S9a and S10a in the ESI†) due to the presence of only even power terms in the fitted polynomial,⁷⁷ unlike from the traditional JT model.

Once the first principle based accurate diabatic PESs for the NO₂ radical are in hand, we have carried out nuclear dynamics to generate envelops of X²A₁ and A²B₂ states in the photodetachment

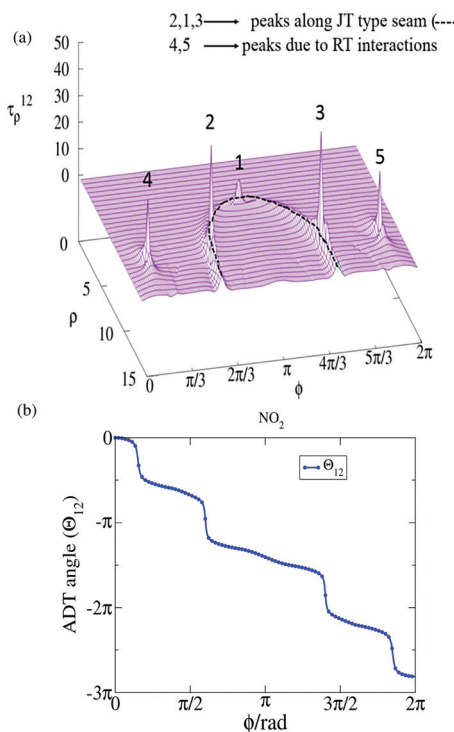


Fig. 9 For the Q_1-Q_3 pair of the NO_2 radical, (a) τ_p^{12} exhibits singularities along the semicircular JT type seam (peaks 1 to 3) and in the RT regions (peaks 4 and 5) over $\rho-\phi$ configuration space. Panel (b) shows 1D variation of the ADT angle, Θ_{12} along ϕ coordinate keeping the ρ fixed at 10.7, which acquires the numerical value of 3π due to the JT and RT couplings.

spectrum. In order to compute the spectra, dynamical calculations are performed at the close vicinity of the equilibrium geometry (FC region), where the molecular vibrations can be represented by linearly independent normal mode coordinates. Hence, a product type wavefunction with Gaussian wave packets (GWPs) for each normal mode of NO_2^- is considered as the initial wavefunction while solving the time dependent SE. While performing the dynamics,^{90,134–138} we have computed time dependent nuclear wavefunctions, calculated the autocorrelation function at different times and carried out its Fourier transformation to generate the photodetachment spectra of the NO_2^- anion (see the details in Section S9 of the ESI†)

We have placed the initial wavepacket of NO_2^- on each of the electronic states, $\tilde{\chi}^2\text{A}_1$ and $\tilde{\Lambda}^2\text{B}_2$ of the neutral species to execute two different dynamical calculations and the overall spectral profile⁷⁷ shows a satisfactory agreement with the experimental one measured by Weaver *et al.*⁹⁴ (see Fig. 10). It is interesting to note that the asymmetric stretching mode (Q_3) is mainly responsible for vibronic transitions in the spectral profile, whereas the peak progressions are governed by the symmetric bending (Q_1) and stretching (Q_2) vibrations. Further calculation has revealed that the absence of a Q_2 normal mode broadens the spectral band of an $\tilde{\chi}^2\text{A}_1$ state.⁷⁷ Our theoretical findings clearly establish the effects of JT and RT couplings to the overall nonadiabaticity of NO_2 and the photodetachment spectra of its anionic counterpart.⁷⁷

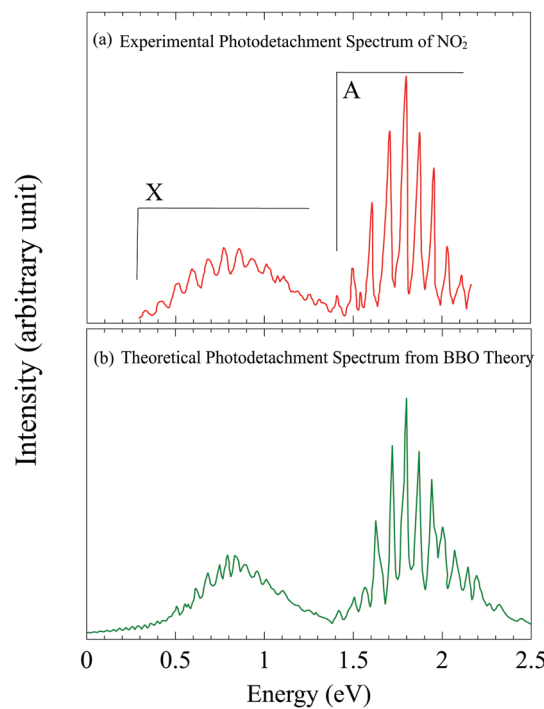


Fig. 10 Our BBO calculated spectrum (panel (b)) considering all non-adiabatic interactions (JT and RT couplings) is compared with the experimental one (panel a).⁹⁴ The results are adopted from ref. 77.

8.2 Molecular system with three coupled electronic states: Na_3 cluster

In order to establish the workability of BBO based diabatic PESs for a three coupled electronic manifold, we have analysed the effects of JT and PJT couplings on the spectral profiles of prototypical alkali trimers, Na_3 and K_3 . Several theoretical^{124,139–144} as well as experimental^{95,145} studies on these triatomic clusters were carried out over the last thirty years especially due to their simple electronic structure and presence of only three vibrational modes. For the Na_3 cluster, our group has performed dynamical investigation employing the model diabatic Hamiltonian constructed by Cocchini *et al.*,^{124,125} where BO, EBO and diabatic surfaces have been used to predict the theoretical spectrum. Later on, we have pursued *ab initio* electronic structure calculations to generate first principle based adiabatic PESs and NACTs of three excited electronic states ($2^2\text{E}'$ and $1^2\text{A}'_1$) with MRCI methodology as implemented in MOLPRO.¹⁰⁵ The highly accurate diabatic PESs⁷⁷ have been computed over a 2D nuclear plane ($\rho-\phi$) comprising bending (Q_x) and asymmetric stretching (Q_y) modes at a specific value of symmetric stretching (Q_z) coordinate (3.7 Å). It is clearly evident from our calculation that the Na_3 cluster possesses accidental CIs within two branches of $2^2\text{E}'$ state as well as PJT interaction among the $2^2\text{E}'$ and $1^2\text{A}'_1$ states. Among the accidental CIs, three are located at a C_{2v} geometry, but the remaining three merge at the D_{3h} point leading to a total of four CIs over the nuclear CS.⁷⁷

8.2.1 Model diabatic Hamiltonian of the Na_3 cluster. We have considered the following model form of the diabatic Hamiltonian proposed by Cocchini *et al.*¹²⁴ over the polar plane

$(\rho-\phi)$ of Q_x and Q_y for the three excited states ($2^2E'$ and $1^2A'_1$) of the Na_3 cluster:

$$V^{\text{dia}}(\rho, \phi) = \begin{pmatrix} \frac{\rho^2}{2} + U_2 & U_1 & W_1 - W_2 \\ U_1 & \frac{\rho^2}{2} - U_2 & W_1 + W_2 \\ W_1 - W_2 & W_1 + W_2 & \varepsilon_0 + \frac{\rho^2}{2} \end{pmatrix}, \quad (58)$$

where

$$U_1(\rho, \phi) = K\rho \cos \phi + \frac{1}{2}g\rho^2 \cos(2\phi)$$

$$U_2(\rho, \phi) = K\rho \sin \phi - \frac{1}{2}g\rho^2 \sin(2\phi)$$

$$W_1(\rho, \phi) = P\rho \cos \phi + \frac{1}{2}f\rho^2 \cos(2\phi)$$

$$W_2(\rho, \phi) = P\rho \sin \phi - \frac{1}{2}f\rho^2 \sin(2\phi)$$

In the above expressions, the nuclear coordinates are converted into their dimensionless forms and thereby, the JT coupling constants [$K (= 4.9)$ and $g (= 0.035)$]¹²⁴ as well as PJT coupling parameters [$P (= 3.46)$ and $f (= 0.025)$]¹²⁴ are also dimensionless. On the other hand, the quantity, $\varepsilon_0 (= 2\Delta)$ controls the energy spacing (Δ) between the second and third states.

At the PJT situation ($K = g = 0$), analytic expressions of ρ and ϕ components of NACTs and the corresponding curls are depicted in Section S10 of the ESI.[†] It is clear from the analytic expressions of curl (curl $\tau_{\rho\phi}^{12}$, curl $\tau_{\rho\phi}^{13}$ and curl $\tau_{\rho\phi}^{23}$) that those quantities vanish identically at $\Delta = 0$ for three-state degeneracy between A and E states. On the other hand, if the gradient of numerically calculated ADT angles is used to compute such equations, those curls appear to be negligibly small (curl $\tau \approx 0$) up to certain nonzero Δ ($\leq 172 \text{ cm}^{-1}$).

At a very low value of Δ ($\leq 172 \text{ cm}^{-1}$), curl τ is very close to zero (0) and therefore, the EBO equations can be formulated. At this junction, one can implement classical forbidden conditions for each electronic state from others at and around a specific energy, *i.e.*, $|\psi_i| \gg |\psi_j| (i \neq j)$ and derive the single-surface EBO equations as,

$$-\frac{\hbar^2}{2m} \left\{ \left(\frac{\partial}{\partial \rho} + i\omega_\rho \right)^2 + \frac{1}{\rho} \left(\frac{\partial}{\partial \rho} + i\omega_\rho \right) + \frac{1}{\rho^2} \left(\frac{\partial}{\partial \phi} + i\omega_\phi \right)^2 \right\} \Phi_1 + (u_1 - E) \Phi_1 = 0, \quad (59a)$$

$$-\frac{\hbar^2}{2m} \left\{ \frac{\partial^2}{\partial \rho^2} + \frac{1}{\rho} \frac{\partial}{\partial \rho} + \frac{1}{\rho^2} \frac{\partial^2}{\partial \phi^2} \right\} \Phi_2 + (u_2 - E) \Phi_2 = 0, \quad (59b)$$

$$-\frac{\hbar^2}{2m} \left\{ \left(\frac{\partial}{\partial \rho} - i\omega_\rho \right)^2 + \frac{1}{\rho} \left(\frac{\partial}{\partial \rho} - i\omega_\rho \right) + \frac{1}{\rho^2} \left(\frac{\partial}{\partial \phi} + i\omega_\phi \right)^2 \right\} \Phi_3 + (u_3 - E) \Phi_3 = 0, \quad (59c)$$

where the components of non-zero NACM eigenvalue (ω_ρ and ω_ϕ) take the following form:

$$\omega_\rho = \frac{A_0}{2w}, \quad \omega_\phi = \frac{A_2}{2w}.$$

with $A_0 = Pf\rho^2 \sin(3\phi)$, $A_2 = 2P^2\rho^2 - f^2\rho^4 - Pf\rho^3 \cos(3\phi)$ and $w = P^2\rho^2 + \frac{1}{4}f^2\rho^4 + Pf\rho^3 \cos(3\phi)$. The calculated GI for the angular component of the eigenvalue (ω_ϕ) has been found to be gauge invariant ($\int_0^{2\pi} \omega_\phi d\phi = 2\pi$, as expected for three state degeneracy), which validates the workability of the EBO equations (eqn (59)) over the chosen domain of nuclear CS.

We have computed photoabsorption spectra of the lowest state of the above mentioned model system employing ordinary BO, EBO (eqn (59a)) and diabatic SEs (eqn (58)) with $\Delta = 0$ and 172 cm^{-1} , which are displayed in Fig. 11. An excellent concurrence can be observed between the spectral envelops obtained from EBO and diabatic surfaces at $\Delta = 0$,¹²⁵ whereas these profiles exhibit an approximate agreement for a $\Delta = 172 \text{ cm}^{-1}$ case. In contrast, spectral bands arising from an ordinary BO equation show large deviations from the diabatic ones for both the situations ($\Delta = 0$ and 172 cm^{-1}).

8.2.2 BBO theory based diabatic Hamiltonian of the Na_3 cluster. While carrying out BBO theory based diabatization of three excited states ($2^2E'$ and $1^2A'_1$) of the Na_3 cluster, the adiabatic PESs and MS adapted NACTs (see Subsection S6 of the ESI[†] for details) have been plugged into the ADT equations^{3,86} for three state electronic manifold (see Subsection S5.1 of the ESI[†]) and those equations have been numerically integrated over the 2D nuclear planes to calculate the ADT angles. Finally, the

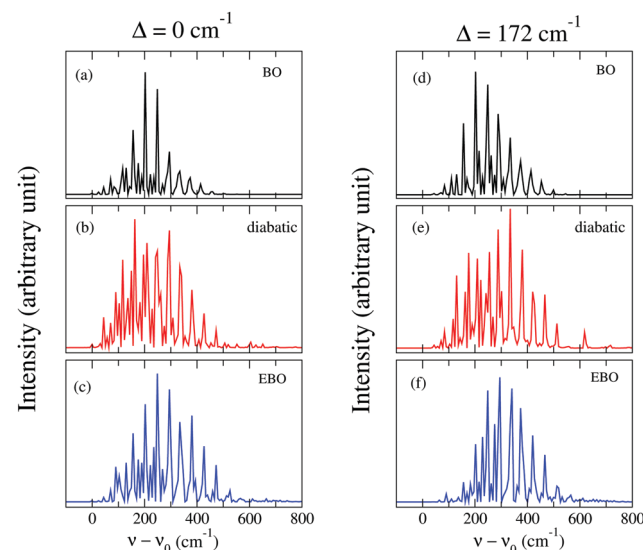


Fig. 11 Panels (a)–(c) describe the photoabsorption spectra of the Na_3 cluster employing ordinary BO equations, diabatic SEs and single-surface EBO equations, respectively for $\Delta = 0$ energy gap between E' and A'_1 states. On the other hand, panels (d)–(f) represent the same quantities for $\Delta = 172 \text{ cm}^{-1}$. For the first case ($\Delta = 0$), one can observe a good agreement between the EBO and diabatic spectral profiles, but they match approximately for $\Delta = 172 \text{ cm}^{-1}$. In contrast, BO profiles exhibit substantial deviation from the diabatic ones. The results are taken from ref. 125.

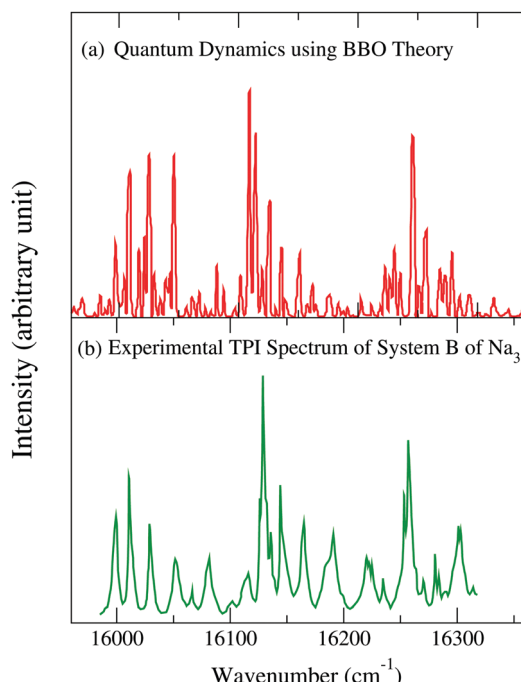


Fig. 12 The diagram depicts a comparison of the absorption spectrum for system B of the Na_3 cluster obtained from BBO based diabatic surfaces [panel (a)] with the experimental two-photon ionization spectrum⁹⁵ [panel (b)]. This figure has been adopted from ref. 30.

resulting ADT matrices have been employed to construct a single-valued, smooth and continuous diabatic Hamiltonian for the Na_3 cluster. In addition, it has been observed that along the Q_y normal mode, the diabatic coupling elements show symmetric functional forms (see Fig. S9b and S10b in the ESI†), which only include even power polynomials of Q_y coordinate.^{30,84}

Once the diabatic PESs and couplings are in hand, we have carried out nuclear wave packet dynamics over the Q_x-Q_y plane using the GWP as the time-independent solution of the unperturbed Hamiltonian [$\hat{H}_0(Q_x, Q_y) = \hat{T}_{\text{nuc}} + (1/2)(Q_x^2 + Q_y^2)$]. The dynamical calculations have been performed over the diabatic surfaces employing an FFT-Lanczos method to compute the auto-correlation function, $C(t)$ s (see eqn (S95) in Section S9 of the ESI†) and such function has been Fourier transformed to generate the theoretical spectral profile. Three different calculations have been executed to generate individual state spectra of $2^2\text{E}'$ and $1^2\text{A}'_1$, and finally, all three spectra have been convoluted to obtain the overall spectral envelop.³⁰ The experimental two-photon ionization (TPI) spectrum for system B of the Na_3 cluster⁹⁵ is well reproduced by our calculations as demonstrated in Fig. 12. Moreover, it has been observed that the diabatic population profiles cross each other as a function of time verifying the existence of CIs between those states.³⁰

8.3 Molecular systems with five coupled electronic states: NO_3 radical and Bz^+ radical cation

Nitrate radical (NO_3) and benzene radical cations (Bz^+) are two representative examples, which have drawn attention over the past few decades due to the highly structured spectral bands of

the NO_3^- anion and C_6H_6 molecule. In this context, we have developed explicit expressions of ADT equations in terms of mixing angles between the states for five electronic state SHS (see Subsection S5.3 of the ESI†).⁸⁰

8.3.1 NO_3 radical. A NO_3 radical exhibits highly complex spectral features due to intense vibronic coupling between its low-lying five electronic states, $\tilde{\text{X}}^2\text{A}'_2$ (1^2B_2), $\tilde{\text{A}}^2\text{E}''$ (1^2A_2 and 1^2B_1) and $\tilde{\text{B}}^2\text{E}'$ (1^2A_1 and 2^2B_2), which lie within a small energy range of 2 eV. Several theoretical predictions^{53,54,80–82,103,146–148} were proposed to elucidate the underlying physics of the complex spectral envelop obtained from various experimental observations, like dispersed fluorescence spectroscopy,^{149,150} Fourier-transform infrared spectroscopy,^{151,152} photoelectron spectroscopy⁹⁶ and also from cavity ringdown spectroscopy (CRDS)^{153,154} experiments. Adhikari *et al.*^{80,81} have depicted that strong JT interactions prevail within the $\tilde{\text{A}}^2\text{E}''$ and $\tilde{\text{B}}^2\text{E}'$ states at an equilibrium D_{3h} point along with accidental CIs at C_s and C_{2v} geometries within '3–4' and '4–5' electronic states. On the other hand, NO_3 possesses significant PJT coupling between $\tilde{\text{X}}^2\text{A}'_2$ and $\tilde{\text{B}}^2\text{E}'$ states.^{80,81} Due to those effects, various controversies appeared about the ground state equilibrium geometry of this radical, but finally Eisfeld and Morokuma confirmed it to be of D_{3h} symmetry.¹⁰³

Our group has performed a detailed investigation of all the important nonadiabatic interactions present over the nuclear planes composed of symmetric stretching (Q_1), umbrella (Q_2) and degenerate asymmetric stretching (Q_{3x} and Q_{3y}) modes.^{80,81} We have computed adiabatic PESs and NACTs as functions of polar transformed coordinates (ρ and ϕ) of each normal mode pair (Q_i and Q_j) employing an MRCI level of calculation in a MOLPRO quantum chemistry package.¹⁰⁵ Those *ab initio* calculated NACTs have been plugged into the ADT equations for five-state SHS (see Subsection S5.3 of the ESI†) to obtain the mixing angles at each nuclear configuration over those 2D planes.⁸² It is evident from Fig. 13 that angular variation (ϕ) of ADT angles [$\theta_{23}(Q_{3x}, Q_{3y})$ and $\theta_{45}(Q_{3x}, Q_{3y})$] at fixed ρ (= 4.9) exhibits the quantization properties of NACTs. Those angles acquire the magnitude of π and 4π , respectively, validating the presence of one '2–3' CI (JT CI at D_{3h} point) and four '4–5' CIs (one JT CI at D_{3h} geometry and three accidental CIs at equivalent C_{2v} points) encircled by the closed loop. Similarly, the diagonal elements of ADT matrices, namely, A_{22} [= A_{33}] and A_{44} [= A_{55}] undergo one and four sign inversions, respectively, bearing evidence of the aforementioned CIs. Fig. 13 also reveals that the functional behaviour of ADT angles depends on the nonadiabaticity of the molecule [$\omega_\phi(\phi)$] and thereby, the acquired phase is topological ($e^{\pm i\omega_\phi(\phi)}$) in nature rather than geometric ($e^{\pm in\phi}$)^{27,155,156} (indicated by the dashed lines). In addition to '2–3' and '4–5' CIs, NO_3 exhibits two symmetric C_s CIs over the Q_2-Q_{3x} plane and one C_s CI over the Q_2-Q_{3y} plane.^{80,82} Indeed, ADT matrices lead to smooth, single-valued and continuous diabatic PES matrices over the nuclear CS. It is important to note that along Q_{3x} , the diabatic PESs as well as the couplings can only be fitted with even power polynomial terms (see Fig. S9c and S10c in the ESI†),^{82,88} which differs from the traditional JT model.

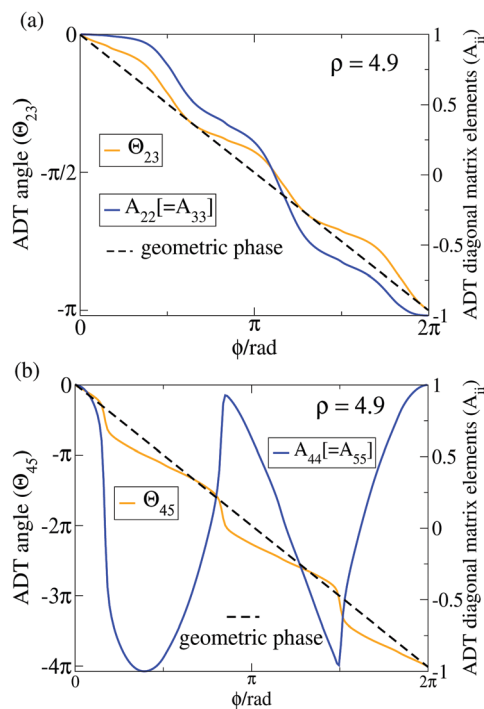


Fig. 13 For the $Q_{3x}-Q_{3y}$ nuclear plane of the NO_3^- radical, 1D variation of (a) Θ_{23} and (b) Θ_{45} along the ϕ coordinate at definite ρ ($= 4.9$) attains the magnitude of π and 4π , respectively due to the presence of one '2–3' JT CI and four '4–5' CIs (one JT along with three accidental ones). On the other hand, (a) $A_{22} [= A_{33}]$ and (b) $A_{44} [= A_{55}]$ bear the signature of the aforementioned CIs by exhibiting one and four sign inversions, respectively.

In order to simulate the photodetachment spectra of a NO_3^- anion, we carry out dynamical calculations on the BBO theory based diabatic PESs of five electronic states. The autocorrelation functions ($C(t)$ s) are computed from the time-dependent wavefunction obtained from the initial wavepacket constituted with the product of GWP for each normal mode of NO_3^- and then, the spectral envelop has been evaluated by Fourier transformation of $C(t)$ s. Five different dynamical calculations have been performed by placing the initial wave packet of NO_3^- at each of the electronic states of the radical (either $\tilde{\chi}^2\text{A}'_2$ or $\tilde{\Lambda}^2\text{E}''$ or $\tilde{\Lambda}^2\text{E}'$) to convolute the overall spectral profile. Fig. 14 shows good agreement of peak positions, intensity patterns and higher energy progressions of our theoretical spectrum for the E'' state⁸² with the experimental outcome,⁹⁶ nevertheless some discrepancies arise due to the hot bands. The complex profile of the E'' state is very rich with $\text{A}'_2 \rightarrow \text{E}''$ dipole forbidden transitions among which some of them are originated due to an umbrella mode, Q_2 . On the other hand, JT distortion due to Q_3 vibrations, more specifically along the Q_{3y} normal mode and other symmetry allowed accidental CIs develop some anharmonicity in the PESs and hence, those are also responsible for many dipole forbidden transitions. In order to get the details for the dynamical aspects, one may go through Table 2 of ref. 82.

8.3.2 Bz⁺ radical cation. A Bz⁺ radical cation can be considered as one of the challenging molecular species exhibiting highly complex spectral features due to intense vibronic coupling

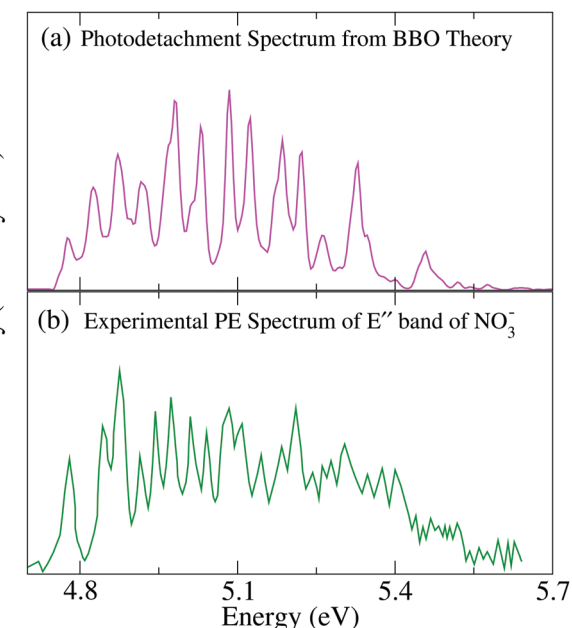


Fig. 14 The upper panel (a) depicts the theoretically computed photo-electron spectrum of the NO_3^- anion obtained from BBO theory based diabatic PESs for E'' states of the neutral counterpart, and it is compared with the experimental outcome⁹⁶ (panel b). The peak positions and the intensity patterns of the computed spectral profile are found to be in accordance with the experimental one. The results are adapted from ref. 82.

between its low-lying five electronic states ($\tilde{\chi}^2\text{E}_{1g}$, $\tilde{\Lambda}^2\text{E}_{2g}$ and $\tilde{\Lambda}^2\text{A}_{2u}$). Several theoretical treatments^{50,51,157–161} were performed to explore dynamical studies considering nonadiabatic interactions present within those states. The low lying doublet states of Bz⁺, namely, $\tilde{\chi}^2\text{E}_{1g}$ and $\tilde{\Lambda}^2\text{E}_{2g}$ show profound JT distortion along the e' modes.^{50,80} In addition, strong PJT couplings and accidental CIs are found within $\tilde{\Lambda}^2\text{E}_{2g}$ and $\tilde{\Lambda}^2\text{A}_{2u}$ electronic states over the FC region of nuclear CS.^{80,157}

Our group carried out dynamical calculations and predicted the theoretical photoelectron spectra of a benzene molecule employing the model diabatic Hamiltonian.^{158–160} Recently, we are pursuing extensive *ab initio* electronic structure calculations to generate adiabatic PESs and NACTs for constructing first principle based highly accurate diabatic PESs of the lowest five electronic states ($\tilde{\chi}^2\text{E}_{1g}$, $\tilde{\Lambda}^2\text{E}_{2g}$ and $\tilde{\Lambda}^2\text{A}_{2u}$). *Ab initio* calculations are performed over the nuclear CS consisting of six normal modes, *i.e.*, breathing (Q_2), degenerate in-plane asymmetric stretching (Q_{16x} and Q_{16y}), degenerate in-plane bending (Q_{18x} and Q_{18y}) and one component of degenerate out-of-plane bending (Q_{19x}) modes. The five state ADT equations (see Subsection S5.3 of the ESI†) are solved numerically to compute the mixing angles followed by construction of ADT matrices and diabatic potential energy matrices.^{80,104} Fig. 15a presents angular variation of ADT angles (Θ_{ij}) of a Bz⁺ radical cation at various fixed ρ -values, which validates the presence of JT as well as accidental CIs encapsulated by the circular contour. For $Q_{16x}-Q_{16y}$ nuclear CS, Θ_{12} and Θ_{34} show the existence of '1–2' and '3–4' JT CIs at a D_{6h} point, whereas over the $Q_{19}-Q_{16x}$ plane,

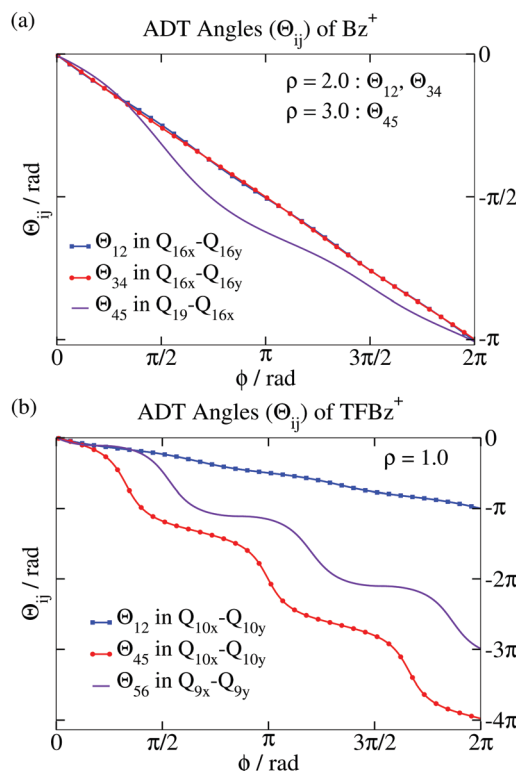


Fig. 15 The upper (a) and lower (b) panels demonstrate 1D variation of ADT angles (Θ_{ij}) of Bz^+ and $TFBz^+$ radical cations along the angular coordinate, ϕ at various ρ -values, which exhibits quantization over different nuclear CSs constituted with the normal mode coordinates.

Θ_{45} exhibits the signature of one accidental '4-5' CI. The diabatic PESs and couplings computed from those ADT angles display symmetric functional behaviour along Q_{16x} (see Fig. S9d and S10d in the ESI†) and Q_{18y} normal modes, which can only be fitted with even power polynomials^{84,85,88} in contrast to a traditional JT model. Our future work is to include additional JT active normal modes in our study and compute the photoelectron spectra of the neutral analogue (Bz) using time-dependent discrete variable representation (TDDVR) dynamics over the BBO constructed diabatic surfaces.¹⁰⁴

8.4 Molecular system with six coupled electronic states: $TFBz^+$ radical cations

The intense vibronic couplings prevailing within the low-lying six electronic states of the $TFBz^+$ radical cation, namely, \tilde{X}^2E'' , \tilde{A}^2A_2'' , \tilde{B}^2E' and \tilde{C}^2A_2' in the FC region are the key mechanistic elements for dictating the position and width of the bands in the photoelectron spectrum.^{98,162} Several research groups^{163–165} selectively chose the neutral analogue of this radical cation to explore the impact of fluorine substitution during the emission process from the excited states as well as to study the JT and PJT effects, which have substantial implications on the dynamical process. Recently, it has been unveiled that among the lowest six electronic states, \tilde{X}^2E'' and \tilde{B}^2E' encounter JT splitting resulting in lowering of the symmetry followed by a decrease in energy due to the e' vibrational modes.^{52,83} On the other

hand, e'' modes are responsible for PJT effects, which are more predominant within \tilde{A}^2A_2'' and \tilde{B}^2E' states.⁸³ Like e'' , e' modes are also responsible for $\tilde{X}^2E'' - \tilde{A}^2A_2''$ and $\tilde{B}^2E' - \tilde{C}^2A_2'$ PJT interactions.⁵²

In our investigation, new accidental CIs and seams are identified within \tilde{X}^2E'' , \tilde{B}^2E' and \tilde{C}^2A_2' states over nuclear CS consisting of six vibrational DOFs, namely, degenerate asymmetric C-C stretching (Q_{9x} and Q_{9y}), degenerate symmetric C-C stretching (Q_{10x} and Q_{10y}) and degenerate C-C-C scissoring (Q_{12x} and Q_{12y}) modes. Fig. 15b describes the quantization of ADT angles (Θ_{ij}) of a $TFBz^+$ radical cation at a fixed ρ -value (= 1.0). $\Theta_{12}(Q_{10x},Q_{10y})$ and $\Theta_{45}(Q_{10x},Q_{10y})$ acquire the magnitude of π and 4π , respectively due to the encapsulated '1-2' JT CI, '4-5' JT CI and three '4-5' accidental CIs. On the other hand, $\Theta_{56}(Q_{9x},Q_{9y})$ reaches 3π at the end of closing the contour validating the presence of three accidental '5-6' CIs. Finally, highly accurate smooth, single-valued and continuous diabatic PESs and couplings are obtained using the ADT equations for the six coupled electronic manifold, where again symmetric functional behaviour of diabatic matrix elements along Q_{9x} (see Fig. S9e and S10e in the ESI†), Q_{10y} and Q_{12y} normal modes depict non-traditional JT interaction.^{83–85}

9 Diabatic Hamiltonian and nuclear dynamics for scattering processes

In this section, we present the results of dynamical calculations on scattering processes employing tri-state quasi-Jahn-Teller model Hamiltonians as well as BBO theory based diabatic PESs for realistic triatomic systems. Our investigations on the model systems⁸⁶ are thoroughly analysed in Subsection 9.1, which possess '1-2' and '2-3' CIs either at the same nuclear configuration (model A) or apart from each other (model B). On the other hand, Subsection 9.2 depicts the construction of a BBO based diabatic Hamiltonian⁷⁵ for H_3^+ , which has been employed to carry out multistate reactive scattering dynamics on the $D^+ + H_2$ system⁹⁰ with the help of the coupled 3D time-dependent wave packet approach.¹⁶⁶ Finally, the profound nonadiabatic interactions of the triatomic system, $F + H_2$ ^{79,91} are discussed in Subsection 9.3.

9.1 Quasi-Jahn-Teller scattering models

In the quasi-Jahn-Teller scattering models, it is assumed that one CI is present between the first two states, and the other one between the second and third states.⁸⁶ In model A, they are placed substantially apart from each other in the nuclear CS so that the model can be treated as two 2×2 BBO systems.⁸⁶ C_2H can be considered as a prototype example for Model A.¹⁶⁷ In contrast, the separation between the CIs vanishes in Model B, which is a 3×3 BBO system.⁸⁶ A typical example may be a Na_3 cluster, where three states (lower and upper $2^2E'$ states and $1^2A_1'$ state) are close to each other to form a 3×3 system.^{30,124} Fig. 16 demonstrates the aforementioned models by presenting 1D variation of the PESs along one nuclear coordinate, namely

x, keeping the value of the other one (*y*) fixed at 0.⁸⁶ It can be clearly observed that the separation between two CIs in model A diminishes to zero (0) in model B and two 2×2 BBO systems turn into a 3×3 system.

9.1.1 Model A. In Model A, two CIs are present at different nuclear configuration points, which is portrayed in Fig. 16a. For this system, the adiabatic PESs are given by:⁸⁶

$$u_1(x, y) = \frac{1}{2}\mu[\omega_0 - \tilde{\omega}_1(x)]^2 y^2 + A_1 \times f_1(x, y),$$

$$u_2(x, y) = \frac{1}{2}\mu\omega_0^2 y^2 - (D_1 - A_1) \times f_1(x, y) + A_1 \times f_2(x, y) + D_1,$$

$$u_3(x, y) = \frac{1}{2}\mu\omega_0^2 y^2 - (D_1 - A_1) \times f_2(x, y) + D_2,$$

$$\tilde{\omega}_1(x) = \omega_1 \exp\left[-\frac{(x - x_0)^2}{\sigma_1^2}\right]$$

$$f_1(x, y) = \exp\left[-\frac{(x - x_0)^2 + y^2}{\sigma^2}\right]$$

$$f_2(x, y) = \exp\left[-\frac{(x + x_0)^2 + y^2}{\sigma^2}\right]$$

where $\mu = 0.58$ amu, $A_1 = 3.0$ eV, $D_1 = 5.0$ eV, $D_2 = 10.0$ eV, $\omega_0 = 39.14 \times 10^{13}$ s⁻¹, $\omega_1 = 7.83 \times 10^{13}$ s⁻¹, $\sigma = 0.3$ Å, and

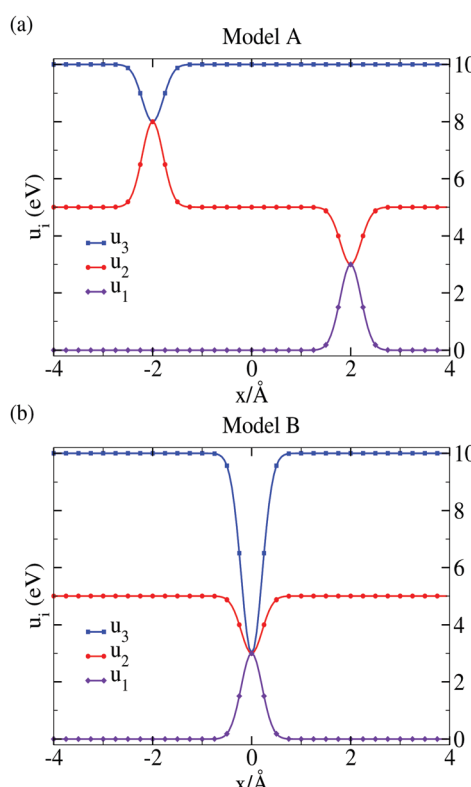


Fig. 16 1D cuts of adiabatic PESs at a fixed *y* value (= 0.0 Å) are presented for (a) model A, where two conical intersections (CIs) are widely apart, and (b) model B, where two CIs merge at the same nuclear configuration.

$\sigma_1 = 0.75$ Å. In Model A, two CIs are separated by $2x_0$ Å, which becomes zero (0) for Model B (3×3 BBO system).

On the other hand, the model forms of ADT angles are considered as,

$$\Theta_{12}(x, y) = \frac{1}{2} \tan^{-1}\left(\frac{y}{x - x_0}\right) \quad \Theta_{23}(x, y) = \frac{1}{2} \tan^{-1}\left(\frac{y}{x + x_0}\right)$$

$$\Theta_{13}(x, y) = 0$$

Therefore, only $\nabla\Theta_{12}$ and $\nabla\Theta_{23}$ are non-zero around the first ('1-2') and second ('2-3') CIs, respectively. At the extreme situation ($x_0 \rightarrow \infty$), the eigenvalues (ω) of NACM obey the GI condition ($\oint \omega \cdot d\mathbf{R} = \pi$), which implies the possibility of formulating single-surface EBO equations. We have performed the dynamical calculations for $x_0 \rightarrow \infty$ on diabatic as well as EBO surfaces. The computed state-to-state vibrational transition probabilities using EBO surfaces follow the appropriate symmetry (even → odd or odd → even) and show good agreement with the corresponding diabatic ones (see Table 3).

9.1.2 Model B. In Model B, '1-2' and '2-3' CIs collapse to form a three-state degeneracy and therefore, it depicts the coupling of three BO states at a single nuclear configuration point shown in Fig. 16b. The adiabatic PESs of such a model take the following form:⁸⁶

$$u_1(x, y) = \frac{1}{2}\mu[\omega_0 - \tilde{\omega}_1(x)]^2 y^2 + A_1 \times f(x, y),$$

$$u_2(x, y) = \frac{1}{2}\mu\omega_0^2 y^2 - (D_1 - A_1) \times f(x, y) + D_1,$$

$$u_3(x, y) = \frac{1}{2}\mu\omega_0^2 y^2 - (D_2 - A_1) \times f(x, y) + D_2,$$

with

$$\tilde{\omega}_1(x) = \omega_1 \exp\left[-\left(\frac{x}{\sigma_1}\right)^2\right]; \quad f(x, y) = \exp\left[-\frac{x^2 + y^2}{\sigma^2}\right]$$

In order to formulate a meaningful EBO equation and accurate diabatic PESs, the functional forms of the ADT angles are

chosen as, $\Theta_{12} = \Theta_{13} = \Theta_{23} = \frac{1}{2} \tan^{-1}\left(\frac{y}{x}\right)$ leading to the

Table 3 Reactive state-to-state transition probabilities ($v \rightarrow v'$, v and v' are vibrational quantum numbers) at various total energies (E) are presented for diabatic and EBO cases, when '1-2' and '2-3' CIs are widely apart (4.0 Å)

E (eV)	$v \rightarrow v'$				
	$0 \rightarrow 0$	$0 \rightarrow 1$	$0 \rightarrow 2$	$0 \rightarrow 3$	$0 \rightarrow 4$
1.25	0.0005 ^a	0.0274	0.0022	0.0145	0.0004
	0.0008 ^b	0.0217	0.0020	0.0147	0.0007
1.50	0.0008 ^a	0.0300	0.0084	0.0414	0.0021
	0.0040 ^b	0.0300	0.0032	0.0412	0.0123
1.75	0.0002 ^a	0.0357	0.0021	0.0761	0.0016
	0.0006 ^b	0.0357	0.0075	0.0763	0.0049

^a For each total energy (E), the upper row signifies diabatic results.

^b For each total energy (E), the lower one indicates the corresponding EBO ones. The results are adopted from ref. 86.

Table 4 Reactive state-to-state transition probabilities ($v \rightarrow v'$) at various total energies (E) are represented for diabatic and EBO cases, when '1-2' and '2-3' CIs coalesce at the same point

E (eV)	$v \rightarrow v'$					
	$0 \rightarrow 0$	$0 \rightarrow 1$	$0 \rightarrow 2$	$0 \rightarrow 3$	$0 \rightarrow 4$	$0 \rightarrow 5$
1.25	0.0227 ^a	0.0000	0.0677	0.0000	0.0061	
	0.0228 ^b	0.0035	0.0727	0.0131	0.0090	
1.50	0.0314 ^a	0.0000	0.0391	0.0000	0.0905	0.0000
	0.0384 ^b	0.0030	0.0704	0.0017	0.0898	0.0060
1.75	0.0250 ^a	0.0000	0.0562	0.0000	0.1280	0.0000
	0.0251 ^b	0.0006	0.0590	0.0012	0.1388	0.0179

^a For each total energy (E), the upper row represents diabatic results.

^b For each total energy (E), the lower one signifies the corresponding EBO ones. The results are adopted from ref. 86.

eigenvalue of NACM, $\omega = \nabla\Theta_{12}\sqrt{3 + 2\sin\Theta_{12}}$. This eigenvalue is found to be gauge invariant for the three-state CI, *i.e.* $\oint \omega \cdot d\mathbf{R} \approx 2\pi$. Finally, the calculated state-to-state vibrational transition probabilities using EBO equations as well as diabatic SEs are presented in Table 4, which shows that the EBO results obey correct symmetry (even \rightarrow even or odd \rightarrow odd) and exhibit satisfactory agreement with the diabatic ones.

9.2 Triatomic reactive system with three coupled electronic states: $\text{H}^+ + \text{H}_2$

In order to scrutinize the competence of BBO theory based diabetization especially in the realm of reaction dynamics, singlet H_3^+ is chosen as a prototype example. This cationic species has appeared as the center of attraction in the community over the past few decades mainly due to the experimental evidence as a molecular species¹⁶⁸ and its immense importance in the interstellar reactions. Because of its electronic simplicity, very accurate ground electronic state PESs^{169,170} with relativistic corrections¹⁷¹ were already probed, but the inclusion of excited states is necessary to explore the reaction dynamics over a wide range of collisional energies. Indeed, the contributions of excited states are included in the global PESs generated by Preston-Tully,¹⁷² Kamisaka-Bian-Nobusada-Nakamura (KBN) surface¹⁷³ and the double many-body expansion (DMBE)¹⁷⁴ potential surface. We have diabetized the *ab initio* calculated adiabatic PESs and NACTs of the three lowest electronic states ($1^1\text{A}'$, $2^1\text{A}'$ and $3^1\text{A}'$),⁷⁵ which have been used to monitor the course of the reaction, $\text{D}^+ + \text{H}_2$ to calculate the integral cross sections (ICS)⁹⁰ of various competing quantum processes. Our investigations on H_3^+ strongly affirms the validity of first principle based BBO theory not only in FC but also in the asymptotic domain of nuclear CS.

9.2.1 Diabatic Hamiltonian for the $\text{H}^+ + \text{H}_2$ system. We have calculated *ab initio* adiabatic PESs and NACTs⁷⁵ in Jacobi coordinates as well as hyperspherical coordinates employing the MRCI level of methodology as implemented in MOLPRO¹⁰⁵ quantum chemistry software. It is evident from the numerically computed NACTs that there exist one '2-3' ($2^1\text{A}'$ and $3^1\text{A}'$) D_{3h} CI and three accidental '1-2' ($1^1\text{A}'$ and $2^1\text{A}'$) C_s seams passing through C_{2v} points. In order to locate the D_{3h} CI between the excited states ($2^1\text{A}'$ and $3^1\text{A}'$), we have performed 1D *ab initio* and ADT calculation in Jacobi coordinates along a closed circular

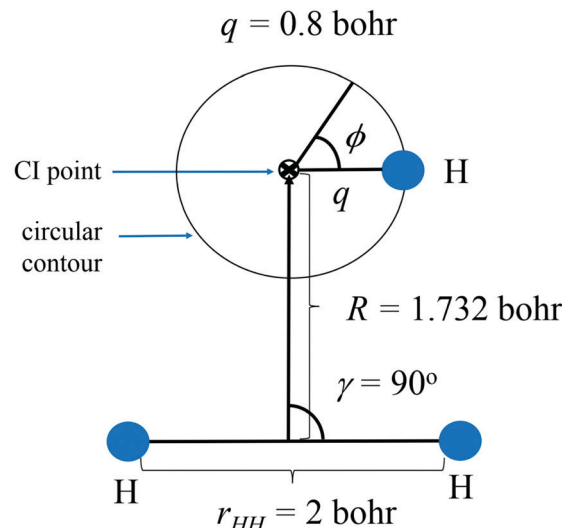


Fig. 17 In the above arrangement, r_{HH} (H–H distance), R (distance from the center of closed contour to the center of mass of H–H) and γ (the angle between r and R) are considered as 2 bohr, 1.732 bohr and 90° , respectively, where the third H atom is traversing along a circular contour of radius, $q = 0.8$ bohr.

path of specific radius, $q = 0.8$ bohr, where r_{HH} (H–H distance), R (distance from the center of closed contour to the center of mass of H–H) and γ (angle between r_{HH} and R) are fixed at 2 bohr, 1.732 bohr and 90° , respectively (see Fig. 17). The resulting ADT angle as presented in Fig. 18a exhibits the quantization property by acquiring the magnitude of π at $\phi = 2\pi$. On the other hand,

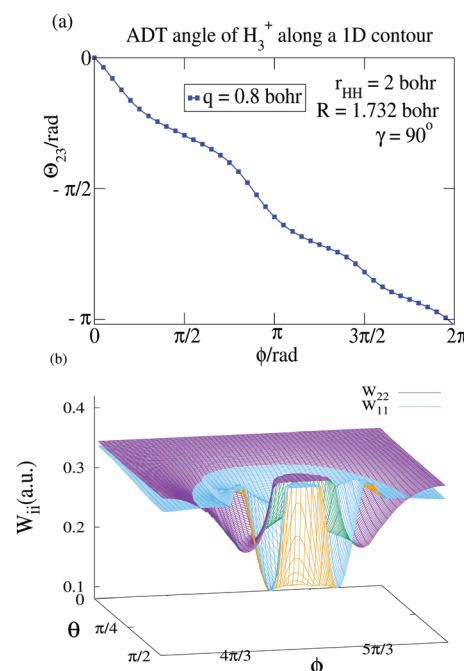


Fig. 18 The upper panel (a) depicts angular variation of θ_{23} , which attains the magnitude of π at $\phi = 2\pi$ showing the presence of '2-3' CI inside the contour. The lower panel (b) portrays diabatic PESs, W_{11} and W_{22} over the θ – ϕ space at $\rho = 10.0$ bohr.^{75,85}

highly accurate global diabatic potential matrix elements have been computed over the nuclear planes consisting of hyperangles ($\theta-\phi$) for each fixed hyperradius ρ , which show smooth, single-valued and continuous functional variation over the nuclear CS.⁷⁵ Fig. 18b depicts diabatic PESs of two low-lying electronic states within the range $\phi = 210^\circ$ to 330° , which shows that the two surfaces cross each other through the semicircular '1-2' C_s seam passing through the C_{2v} point.

9.2.2 Reactive scattering dynamics on multistate $D^+ + H_2$ system. The BBO theory based *ab initio* constructed diabatic PESs have been employed to carry out multistate reactive scattering dynamics on the $D^+ + H_2$ system using couple 3D time-dependent wave packet (TDWP) methodology. We have investigated the following competing processes, namely, reactive non-charge transfer (RNCT), non-reactive charge transfer (NRCT) and reactive charge transfer (RCT):



Our aim is to compute cross sections and rate coefficients of the above processes using the newly constructed diabatic PESs, and to compare these quantities with available experimental findings as well as other theoretical results. We have calculated those observables with our in house dynamics code,¹³⁷ where mixed Open Multi-Processing (OpenMP) – Message Passing Interface (MPI) parallelization scheme^{90,175} has been implemented to reduce the computational cost enormously. The details of the initial wave packet, equation of motion for the time propagation of the scattering wave packet and projection on the asymptotic states are elaborately illustrated in Section S11 of the ESI.† A concise analysis of the total reaction probability and total integral cross section (ICS) of the above three processes is presented in the following paragraphs, which validates the workability of BBO theory^{30,80,86} to construct diabatic PESs as well as highlights the competence of our quantum dynamics^{137,175–178} methodology for multistate scattering processes.

Fig. 19 presents total reaction probabilities ($P(E_{\text{col}})$) in the collision energy (E_{col}) range 1.7–2.5 eV for the total angular momentum, $J = 0$ situation.⁹⁰ The presently calculated RNCT probability (see panel-(a) of Fig. 19) exhibits a gradual decreasing trend with the increment of collision energy and interestingly, shows prominent resonances as compared to the earlier theoretical calculations performed by Adhikari, Varandas and co-workers¹³⁷ on the DMBE PES,¹⁷⁹ and by Chu and Han¹⁸⁰ on the KBNN PES.¹⁷³ For the RCT case as presented in panel-(b) of Fig. 19, the present theoretical calculations depict the "correct" threshold value of E_{col} around ~ 1.8 eV, after which the reaction probabilities gradually increase as we move towards the higher collision energy region.⁹⁰ Although this profile shows a good agreement with that of Adhikari, Varandas and co-workers on the DMBE PES,^{137,179} the variation of $P(E_{\text{col}})$ computed by Chu and Han^{173,180} is generally overestimating over the entire energy regime. Moreover, the total reaction probability profile for the NRCT

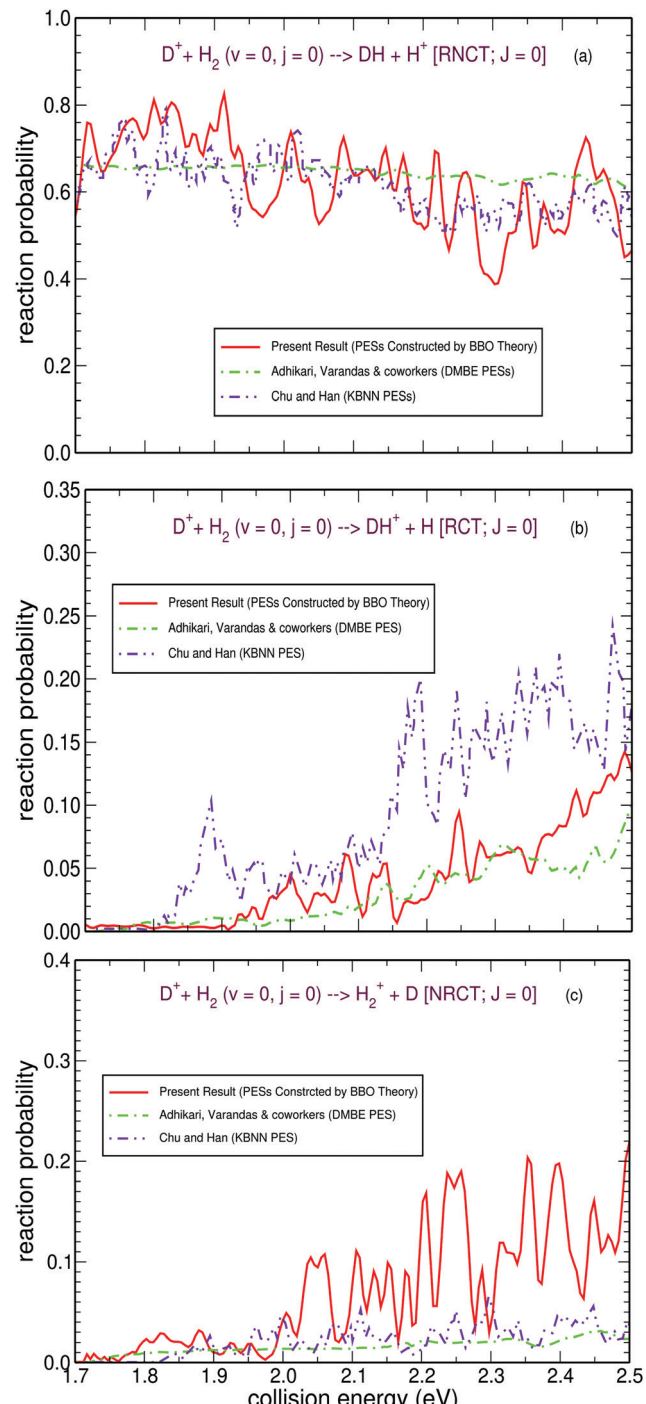


Fig. 19 Total reaction probability as a function of collision energy for (a) RNCT; (b) RCT and (c) NRCT processes of the $D^+ + H_2$ reaction.⁹⁰

process as shown in panel-(c) of Fig. 19 also exhibits negligible magnitude of reaction probability below a specific collision energy (~ 1.8 eV) likewise the case in an RCT process, which indicates the opening of charge transfer processes above a threshold energy. Also for an NRCT process, $P(E_{\text{col}})$ follows a gradual increasing trend with the increment of collision energy.

It is worthwhile mentioning that the diabatic PESs, W_{11} and W_{22} have six crossings along seams both in the reactant and

product channels.⁷⁵ In addition, profound PJT interactions are present within ‘1–3’ and ‘2–3’ states. These nonadiabatic interactions could mainly be attributed for the prominent resonance and other distinct features of the reaction profile as compared to the other theoretical results.

On the other hand, Fig. 20 depicts the variation of total integral cross section (ICS) as a function of collision energy in the regime 1.7–2.5 eV for RNCT, RCT and NRCT processes.

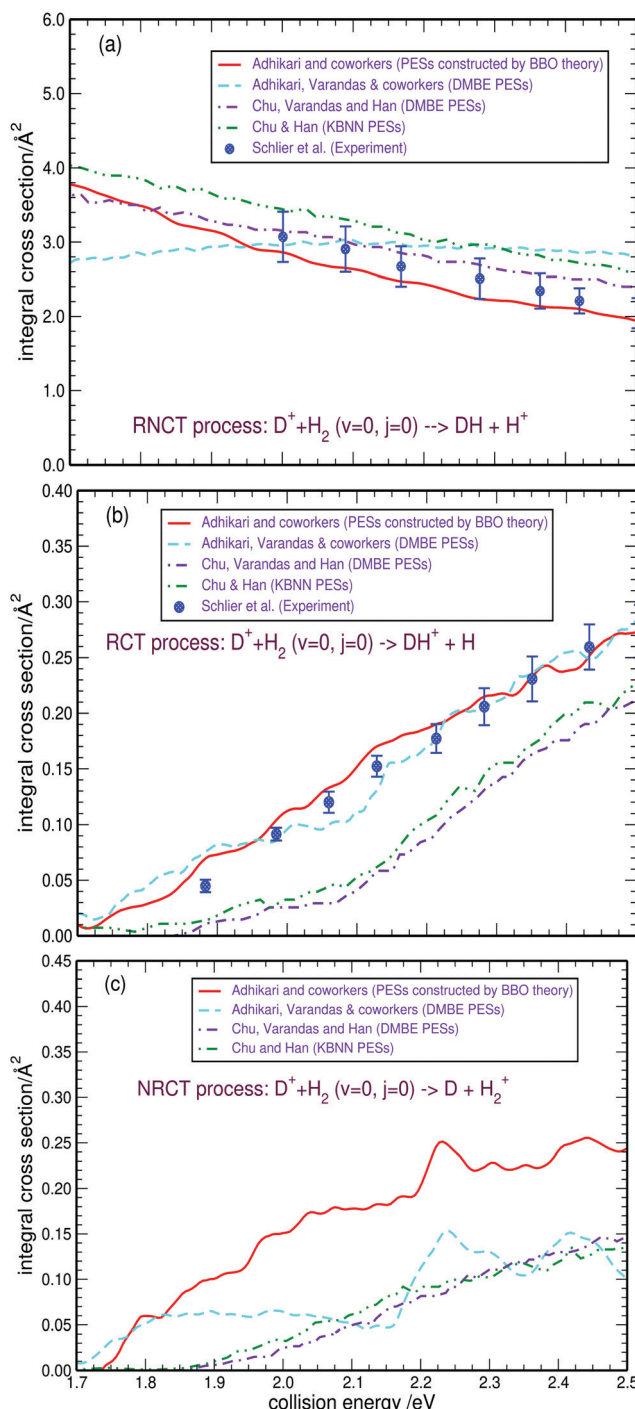


Fig. 20 Total integral cross section as a function of collision energy for (a) RNCT; (b) RCT and (c) NRCT processes of the $D^+ + H_2$ reaction.⁹⁰

The presently calculated profiles⁹⁰ are compared with previous theoretical results obtained by Adhikari, Varandas and co-workers¹³⁷ on DMBE PESs,¹⁷⁹ Chu, Varandas and Han¹⁸¹ on DMBE PESs, and Chu and Han¹⁸⁰ on KBNN PES.¹⁷³ In addition, the available experimental findings of Schlier *et al.*⁹⁹ for RNCT and RCT processes are also presented in the same figure. The ICS profile for the RNCT process (see panel-(a) of Fig. 20) follows a gradual decreasing trend with respect to collision energy and is found to be in excellent agreement with the experimental one.⁹⁹ On the other hand, the magnitudes of ICS for the RCT process (see panel-(b) of Fig. 20) increase gradually with the increment of collision energy beyond the threshold value and such profile shows splendid agreement with the experimental findings by Schlier *et al.*⁹⁹ Like the RCT case, the ICS profile for the NRCT process also shows an increasing trend with respect to collision energy, where very small magnitude of ICS at $E_{\text{col}} < 1.8$ eV indicates the opening of charge transfer processes after the threshold collision energy. To summarize, the RNCT process is the dominant one at the lower collision energy regime, whereas enhanced contribution of charge transfer processes (RCT and NRCT) are observed as we move towards higher collision energy regime.

9.3 Diabatic Hamiltonian for the F + H₂ reactive system

Detailed investigation on the elementary triatomic reaction F + H₂ appears to be one of the most demanding issues over the past few decades due to strong correlation among the electrons, profound spin-orbit (SO) coupling and intense non-adiabatic interactions within low-lying electronic states. During the sixties of the last century onward, several experimental methods^{182–186} have been designed to investigate energy and angular distribution of FH and FD products. Indeed, vibrationally resolved differential cross sections were first measured by Y. T. Lee and his coworkers.^{183,184} The first *ab initio* Bender-O'Neil-Pearson-Schaefer (BOPS) potential was generated by H. F. Schaefer III *et al.*^{187,188} and subsequently, empirical and semiempirical London-Eyring-Polanyi-Sato (LEPS) type PESs were proposed by Muckerman,¹⁸⁹ Takayanagi *et al.*¹⁹⁰ and Truhlar *et al.*^{191,192} to bridge the gap between theoretical and experimental understandings. Nevertheless, such PESs failed to predict correct experimental parameters. On the other hand, Werner and his coworkers^{193–196} computed global adiabatic as well as diabatic PESs with successive upgradation including SO effects and thereby, overcoming many of the shortcomings of previous PESs.

Indeed, many groups have probed the ground state of F + H₂, but studies by including excited states are by far very less. Das *et al.* have explored the JT interaction between the two lowest states of F + H₂ using *ab initio* NACTs and analytically predicted the extent of RT coupling between the upper two excited states.^{197,198} Those studies were limited to the interaction regions of F + H₂ in the vicinity of the CIs.

Recently, our group has been able to construct diabatic PESs by using *ab initio* calculated accurate adiabatic PESs and NACTs of the lowest three electronic states ($1^2A'$, $1^2A''$ and $2^2A'$) for the global manifold of this system.^{79,91} In our study, we have

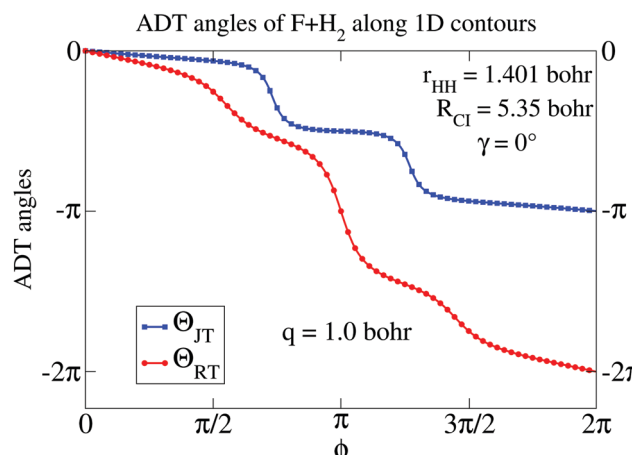


Fig. 21 For the $\text{F} + \text{H}_2$ system, the computed ADT angles corresponding to JT and RT states (Θ_{JT} and Θ_{RT}) attain absolute magnitudes of π and 2π at the end of closed contour integration, respectively, along loops defined in Fig. 7 validating both effects.

numerically validated both JT and RT effects prevailing in this system using the calculated NACTs by showing their quantization along properly chosen contours. The contours along with the coordinates are defined in Fig. 7 in Section 5. At $R_{\text{CI}} = 5.35$ bohr, the JT-type CI between $1^2\text{A}'$ and $2^2\text{A}'$ states along the collinear axis of the diatom is enclosed by the loop shown in Fig. 7a. The calculated ADT angles by close contour integration of NACTs along such paths are depicted in Fig. 21. The angle which couples the two A' states, denoted by Θ_{JT} , reaches a magnitude of π at the end of closed contour integration validating the JT-CI. On the other hand, along the collinear geometries of $\text{F} + \text{H}_2$, the states A' and A'' are degenerate leading to RT interaction. The loop defined in Fig. 7b is such that it encloses the collinear RT seam. Integration along such a contour leads to the value of ADT angle (which couples the two RT states A' and A'' denoted by Θ_{RT}) to 2π at $\phi = 2\pi$, establishing numerically the existence of RT coupling in $\text{F} + \text{H}_2$. We employed the same level of basis set, active space and quantum chemistry methodology (CASSCF/MRCI) to calculate topologically correct ADT angles and construct global diabatic PESs in hyperspherical coordinates. In addition, we have included SO correction to the diabatic PESs which presents a complete description of the $\text{F} + \text{H}_2$ reaction process. The elements of the full diabatic PES matrix are found to be continuous, single-valued, smooth and symmetric which makes them eligible for reactive scattering calculations. In the near future we intend to carry out such calculations to compute reaction probabilities and integral cross sections of this prototype tri-atomic system.

10 Conclusions

In this article, the current perspective of the BBO approach in connection with JT theory has been concisely demonstrated with its implementation on molecular systems important for spectroscopic studies, scattering processes and phase transitions. While constructing the accurate diabatic Hamiltonian employing first principle based BBO theory, one needs adiabatic PESs and

NACTs as essential ingredients. Though both the quantities are physically meaningful, the latter one shows singular and non-analytic functional characteristics around the regions of degeneracy(ies). In order to obtain smooth, continuous and single-valued PESs for stable and precise quantum dynamical calculations, BBO theory is invoked to transform the so-called kinetically coupled adiabatic SE into the diabatic one. Furthermore, in order to explore the behaviours of magnetic compounds with JT active ions (e.g., Mn^{3+} and Cu^{2+}), quantum mechanical treatment for both ground and (much less investigated) excited states has been carried out properly. Such theoretical developments on the nature of the excited state, resulting from electron–nuclear JT coupling, have been carried out within adiabatic approximation and consequently, applied on the satellite electronic transitions of a LaMnO_3 complex.

Section 7 discusses the applicability of the linear JT model in the investigation on special properties of the LaMnO_3 complex during A-type antiferromagnetic order transition below Néel temperature, $T_N \simeq 140$ K. It is significant to reveal that such extended linear JT model predicted the dominant role of the JT splitted cubic perturbed centrifugally stabilized excited state on the origin of higher energy satellite transitions, which display anomalous temperature dependent behaviour at the vicinity of Néel temperature ($T_N \simeq 140$ K) over the 2.2–2.9 eV spectral range of the dielectric function spectra.

In Sections 8 and 9, the workability of BBO theory has been demonstrated for the construction of highly accurate diabatic PESs for spectroscopic and reactive scattering systems. It is important to mention that BBO theory based diabatic coupling elements show symmetric as well as asymmetric functional variation along a specific class of asymmetric stretching or bending modes. Apart from the traditional (linear, bilinear and higher order) JT couplings, such even-power (symmetric) coupling terms are also responsible for nonadiabatic transitions in the photoelectron spectra of various molecular systems. The photo-electron spectra computed from the BBO theory based diabatic PESs of NO_2 and NO_3 radicals exhibit excellent agreement with the experimentally measured ones. Besides spectroscopic calculations, our first principle based diabatization method is also successful to predict accurate reaction probabilities and total ICSs for RNCT, RCT and NRCT channels of the isotopic variants of the $\text{H}^+ + \text{H}_2$ system. Moreover, we have clearly predicted the JT and RT couplings among the $\Sigma-\Pi$ states of the $\text{F} + \text{H}_2$ system and constructed the diabatic PESs for scattering calculations.

It is revealed from our studies that the first principle based BBO formalism is theoretically “exact”, which produces a very accurate realistic diabatic potential energy matrix leading to stable and precise quantum dynamical calculations. In the subsequent studies, our aim is to simulate complex photo-electron spectra of benzene and 1,3,5-trifluorobenzene radical cations (Bz^+ and TFBz^+), which are known for rich JT and PJT vibronic couplings. In addition, we are in the process of performing dynamical calculations on BBO generated global diabatic PESs for the $\text{F} + \text{H}_2$ reaction to reproduce the reaction probabilities and ICSs originating from ground and excited states.

Conflicts of interest

There are no conflicts to declare.

Acknowledgements

JD, SG, BM and SR thank IACS for the research fellowship. SM (file no.: SPM-07/080(0250)/2016-EMR-I) and KN (file no.: 09/080(1068)/2018-EMR-I) acknowledge Council of Scientific and Industrial Research (CSIR), India for funding. SA acknowledges Science and Engineering Research Board (SERB) through project no. CRG/2019/000793 for the research funding and also thanks IACS for the CRAY supercomputing facility.

References

- 1 M. Born and J. R. Oppenheimer, *Ann. Phys.*, 1927, **84**, 457–484.
- 2 M. Born and K. Huang, *Dynamical Theory of Crystal Lattices*, Oxford University Press, Oxford, 1954.
- 3 Z. H. Top and M. Baer, *J. Chem. Phys.*, 1977, **66**, 1363.
- 4 F. Aguilon, M. Sizun, V. Sidis, G. D. Billing and N. Markovic, *J. Chem. Phys.*, 1996, **104**, 4530–4543.
- 5 S. Adhikari and G. D. Billing, *J. Chem. Phys.*, 1999, **111**, 40–47.
- 6 A. J. C. Varandas and Z. R. Xu, *J. Chem. Phys.*, 2000, **112**, 2121–2127.
- 7 B. G. Levine and T. J. Martínez, *Annu. Rev. Phys. Chem.*, 2007, **58**, 613.
- 8 B. F. E. Curchod and T. J. Martínez, *Chem. Rev.*, 2018, **118**, 3305–3336.
- 9 H. Hellmann, *Einführung in die Quantenchemie*, Franz Deuticke, Leipzig, Germany, 1937.
- 10 R. P. Feynmann and A. R. Hibbs, *Quantum Mechanics and Path Integrals*, McCraw-Hill, New York, 1965.
- 11 M. Baer, G. Niedner-Schatterburg and J. P. Toennies, *J. Chem. Phys.*, 1989, **91**, 4169–4182.
- 12 R. Baer, D. M. Charutz, R. Kosloff and M. Baer, *J. Chem. Phys.*, 1996, **105**, 9141–9152.
- 13 D. Grimbart, V. Sidis and V. Cobut, *J. Chem. Phys.*, 1998, **108**, 6331–6341.
- 14 H. A. Jahn and E. Teller, *Proc. R. Soc. London, Ser. A*, 1937, **161**, 220–235.
- 15 J. H. V. Vleck, *J. Chem. Phys.*, 1939, **7**, 72–84.
- 16 H. C. Longuet-Higgins, U. Öpik, M. H. L. Pryce and R. A. Sack, *Proc. R. Soc. London, Ser. A*, 1958, **244**, 1–16.
- 17 U. Öpik and M. H. L. Pryce, *Proc. R. Soc. London, Ser. A*, 1957, **238**, 425–447.
- 18 M. C. M. O'Brien, *Proc. Roy. Soc. A*, 1964, **281**, 323.
- 19 J. C. Slonczewski, *Phys. Rev.*, 1963, **131**, 1596.
- 20 J. Dutta, S. Adhikari and N. Kovaleva, *J. Chem. Phys.*, 2019, **150**, 064703.
- 21 N. N. Kovaleva, K. I. Kugel, Z. Pot(ü)(č)ek, O. E. Kusmartseva, N. S. Goryachev, Z. Brykna, E. I. Demikhov, V. A. Trepakov, A. Dejneka, F. Kusmartsev and A. M. Stoneham, *J. Exp. Theor. Phys.*, 2016, **122**, 890.
- 22 N. N. Kovaleva, A. V. Boris, C. Bernhard, A. Kulakov, A. Pimenov, A. M. Balbashov, G. Khaliullin and B. Keimer, *Phys. Rev. Lett.*, 2004, **93**, 147204.
- 23 N. N. Kovaleva, A. M. Oleš, A. M. Balbashov, A. Maljuk, D. N. Argyriou, G. Khaliullin and B. Keimer, *Phys. Rev. B: Condens. Matter Mater. Phys.*, 2010, **81**, 235130.
- 24 N. N. Kovaleva, J. L. Gavartin, A. L. Shluger, A. V. Boris and A. M. Stoneham, *J. Exp. Theor. Phys.*, 2002, **94**, 178.
- 25 H. C. Longuet-Higgins, *Advances in Spectroscopy*, Interscience Publishers, Ltd, New York and London, 1961, vol. 2.
- 26 H. C. Longuet-Higgins, *Proc. R. Soc. London, Ser. A*, 1975, **344**, 147–156.
- 27 G. Herzberg and H. C. Longuet-Higgins, *Discuss. Faraday Soc.*, 1963, **35**, 77–82.
- 28 C. A. Mead and D. G. Truhlar, *J. Chem. Phys.*, 1982, **77**, 6090–6098.
- 29 A. J. C. Varandas, J. Tennyson and J. N. Murrel, *Chem. Phys. Lett.*, 1979, **61**, 431–434.
- 30 S. Mukherjee, S. Bandyopadhyay, A. K. Paul and S. Adhikari, *J. Phys. Chem. A*, 2013, **117**, 3475–3495.
- 31 J. C. Juanes-Marcos, S. C. Althorpe and E. Wrede, *J. Chem. Phys.*, 2007, **126**, 044317.
- 32 H. Gao, M. Sneha, F. Bouakline, S. C. Althorpe and R. N. Zare, *J. Phys. Chem. A*, 2015, **119**, 12036–12042.
- 33 S. C. Althorpe, J. C. Juanes-Marcos and E. Wrede, *Adv. Chem. Phys.*, 2008, **138**, 1–42.
- 34 S. C. Althorpe, T. Stecher and F. Bouakline, *J. Chem. Phys.*, 2008, **129**, 214117.
- 35 F. Bouakline, S. C. Althorpe and D. P. Ruiz, *J. Chem. Phys.*, 2008, **128**, 124322.
- 36 W. D. Hobey and A. D. McLachlan, *J. Chem. Phys.*, 1960, **33**, 1695–1703.
- 37 F. T. Smith, *Phys. Rev.*, 1969, **179**, 111–123.
- 38 M. Baer, *Chem. Phys. Lett.*, 1975, **35**, 112–118.
- 39 M. Baer, *Phys. Rep.*, 2002, **358**, 75–142.
- 40 M. Baer, *Beyond Born–Oppenheimer: Conical intersections and Electronic nonadiabatic coupling terms*, Wiley Interscience, New Jersey, 2006.
- 41 M. Baer and R. Englman, *Mol. Phys.*, 1992, **75**, 293–303.
- 42 A. Alijah and M. Baer, *J. Phys. Chem. A*, 2000, **104**, 389–396.
- 43 B. K. Kendrick, C. A. Mead and D. G. Truhlar, *Chem. Phys.*, 2002, **277**, 31–41.
- 44 N. Matsunaga and D. R. Yarkony, *Mol. Phys.*, 1998, **93**, 79–84.
- 45 H. Köppel, W. Domcke and L. S. Cederbaum, *Adv. Chem. Phys.*, 1984, **57**, 59–246.
- 46 A. Thiel and H. Köppel, *J. Chem. Phys.*, 1999, **110**, 9371.
- 47 H. Köppel, J. Gronki and S. Mahapatra, *J. Chem. Phys.*, 2001, **150**, 2377.
- 48 H. Köppel and B. Schubert, *Mol. Phys.*, 2006, **104**, 1069.
- 49 S. Mahapatra, H. Köppel and L. Cederbaum, *J. Chem. Phys.*, 1999, **110**, 5691–5701.
- 50 M. Döschner, H. Köppel and P. G. Szalay, *J. Chem. Phys.*, 2002, **117**, 2645–2656.
- 51 H. Köppel, M. Döschner, I. Bâldea, H. D. Meyer and P. G. Szalay, *J. Chem. Phys.*, 2002, **117**, 2657–2671.

- 52 T. Mondal and S. Mahapatra, *Phys. Chem. Chem. Phys.*, 2009, **11**, 10867–10880.
- 53 A. Viel and W. Eisfeld, *J. Chem. Phys.*, 2004, **120**, 4603–4613.
- 54 S. Faraji, H. Köppel, W. Eisfeld and S. Mahapatra, *Chem. Phys.*, 2008, **347**, 110–119.
- 55 A. Viel, W. Eisfeld, S. Neumann, W. Domcke and U. Manthe, *J. Chem. Phys.*, 2006, **124**, 214306.
- 56 S. Bhattacharyya, D. Opalka, L. V. Poluyanov and W. Domcke, *J. Phys. Chem. A*, 2014, **118**, 11962–11970.
- 57 R. J. Hickman, R. A. Lang and T. Zeng, *Phys. Chem. Chem. Phys.*, 2018, **20**, 12312–12322.
- 58 I. Seidu, P. Goel, X. G. Wang, B. Chen, X. B. Wang and T. Zeng, *Phys. Chem. Chem. Phys.*, 2019, **21**, 8679–8690.
- 59 A. Abedi, N. T. Maitra and E. K. U. Gross, *Phys. Rev. Lett.*, 2010, **105**, 123002.
- 60 A. Abedi, N. T. Maitra and E. K. U. Gross, *J. Chem. Phys.*, 2012, **137**, 22A530.
- 61 G. H. Gossel, L. Lacombe and N. T. Maitra, *J. Chem. Phys.*, 2019, **150**, 154112.
- 62 G. A. Worth, H.-D. Meyer, H. Köppel, L. S. Cederbaum and I. Burghardt, *Int. Rev. Phys. Chem.*, 2008, **27**, 569.
- 63 G. W. Richings and S. Habershon, *J. Chem. Phys.*, 2018, **148**, 134116.
- 64 G. W. Richings, I. Polyak, K. Spinlove, G. A. Worth, I. Burghardt and B. Lasorne, *Int. Rev. Phys. Chem.*, 2015, **34**, 269.
- 65 G. W. Richings and G. A. Worth, *J. Phys. Chem. A*, 2015, **119**, 12457.
- 66 G. W. Richings and G. A. Worth, *Chem. Phys. Lett.*, 2017, **683**, 606.
- 67 A. J. C. Varandas, F. B. Brown, C. A. Mead, D. G. Truhlar and N. C. Blais, *J. Chem. Phys.*, 1987, **86**, 6258.
- 68 H. Nakamura and D. G. Truhlar, *J. Chem. Phys.*, 2003, **118**, 6816.
- 69 C. Evenhuis and T. J. Martínez, *J. Chem. Phys.*, 2011, **135**, 224110.
- 70 X. Zhu and D. R. Yarkony, *J. Chem. Phys.*, 2012, **136**, 174110.
- 71 B. Sarkar and S. Adhikari, *J. Phys. Chem. A*, 2008, **112**, 9868–9885.
- 72 A. K. Paul, S. Ray, D. Mukhopadhyay and S. Adhikari, *Chem. Phys. Lett.*, 2011, **508**, 300–305.
- 73 A. K. Paul, S. Ray, D. Mukhopadhyay and S. Adhikari, *J. Chem. Phys.*, 2011, **135**, 034107.
- 74 S. Mukherjee and S. Adhikari, *Chem. Phys.*, 2014, **440**, 106–118.
- 75 S. Mukherjee, D. Mukhopadhyay and S. Adhikari, *J. Chem. Phys.*, 2014, **141**, 204306.
- 76 S. Sardar, S. Mukherjee, A. K. Paul and S. Adhikari, *Chem. Phys.*, 2013, **416**, 11–20.
- 77 S. Mukherjee, B. Mukherjee, S. Sardar and S. Adhikari, *J. Chem. Phys.*, 2015, **143**, 244307.
- 78 B. Mukherjee, S. Mukherjee and S. Adhikari, *J. Phys.: Conf. Ser.*, 2016, **759**, 012050.
- 79 B. Mukherjee, S. Mukherjee, K. R. Shamasundar and S. Adhikari, *J. Phys.: Conf. Ser.*, 2017, **833**, 012004.
- 80 S. Mukherjee, B. Mukherjee and S. Adhikari, *J. Phys. Chem. A*, 2017, **121**, 6314–6326.
- 81 B. Mukherjee, S. Mukherjee, S. Sardar, K. R. Shamasundar and S. Adhikari, *Mol. Phys.*, 2017, **115**, 2833–2848.
- 82 B. Mukherjee, S. Mukherjee, S. Sardar, K. R. Shamasundar and S. Adhikari, *Chem. Phys.*, 2018, **515**, 350–359.
- 83 S. Mukherjee, J. Dutta, B. Mukherjee, S. Sardar and S. Adhikari, *J. Chem. Phys.*, 2019, **150**, 064308.
- 84 B. Mukherjee, K. Naskar, S. Mukherjee, S. Ghosh, T. Sahoo and S. Adhikari, *Int. Rev. Phys. Chem.*, 2019, **38**, 287–341.
- 85 K. Naskar, S. Mukherjee, B. Mukherjee, S. Ravi, S. Mukherjee, S. Sardar and S. Adhikari, *J. Chem. Theory Comput.*, 2020, **16**, 1666–1680.
- 86 B. Sarkar and S. Adhikari, *J. Chem. Phys.*, 2006, **124**, 074101.
- 87 S. Mukherjee, B. Mukherjee, S. Sardar and S. Adhikari, *Comput. Theor. Chem.*, 2019, **1154**, 57–67.
- 88 S. Mukherjee, B. Mukherjee, J. Dutta, S. Sardar and S. Adhikari, *ACS Omega*, 2018, **3**, 12465–12475.
- 89 B. Mukherjee, S. Ghosh and S. Adhikari, *J. Phys.: Conf. Ser.*, 2018, **1148**, 012001.
- 90 S. Ghosh, S. Mukherjee, B. Mukherjee, S. Mandal, R. Sharma, P. Chaudhury and S. Adhikari, *J. Chem. Phys.*, 2017, **147**, 074105.
- 91 B. Mukherjee, K. Naskar, S. Mukherjee, S. Ravi, K. R. Shamasundar, D. Mukhopadhyay and S. Adhikari, *J. Chem. Phys.*, 2020, **153**, 174301.
- 92 E. Renner, *Z. Phys.*, 1934, **92**, 172–193.
- 93 I. B. Bersuker, *The Jahn-Teller Effect*, Cambridge University Press, 2006.
- 94 A. Weaver, R. B. Metz, S. E. Bradforth and D. M. Neumark, *J. Chem. Phys.*, 1989, **90**, 2070–2071.
- 95 W. E. Ernst and O. Golonzka, *Phys. Scr., T*, 2004, **T112**, 27.
- 96 A. Weaver, D. W. Arnold, S. E. Bradforth and D. M. Neumark, *J. Chem. Phys.*, 1991, **94**, 1740–1751.
- 97 P. Baltzer, L. Karlsson, B. Wannberg, G. Öhrwall, D. M. P. Holland, M. A. MacDonald, M. A. Hayes and W. von Niesson, *Chem. Phys.*, 1997, **224**, 95–119.
- 98 R. Gilbert, P. Sauvageau and C. Sandorfy, *Chem. Phys. Lett.*, 1972, **17**, 465–470.
- 99 C. Schlier, U. Nowotny and E. Teloy, *Chem. Phys.*, 1987, **111**, 401–408.
- 100 Y.-R. Tzeng and M. H. Alexander, *J. Chem. Phys.*, 2004, **121**, 5183–5190.
- 101 K. Hirota, N. Kaneko, A. Nishizawa and Y. Endoh, *J. Phys. Soc. Jpn.*, 1996, **65**, 3736–3739.
- 102 J. Rodríguez-Carvajal, M. Hennion, F. Moussa, A. H. Moudden, L. Pinsard and A. Revcolevschi, *Phys. Rev. B: Condens. Matter Mater. Phys.*, 1998, **57**, R3189.
- 103 W. Eisfeld and K. Morokuma, *J. Chem. Phys.*, 2000, **113**, 5587–5597.
- 104 S. Mukherjee, S. Ravi, K. Naskar, S. Sardar and S. Adhikari, *J. Chem. Phys.*, 2020, to be submitted.
- 105 H.-J. Werner, P. J. Knowles, G. Knizia, F. R. Manby, M. Schütz, et al., *MOLPRO, version 2010.1, a package of ab initio programs*, 2010, see <http://www.molpro.net>.
- 106 H. C. Longuet-Higgins, *Mol. Phys.*, 1963, **6**, 445–460.
- 107 P. R. Bunker and P. Jensen, *Molecular symmetry and spectroscopy*, NRC Research Press, 2nd edn, 2006.

- Published on 20 October 2020. Downloaded by Indian Association for the Cultivation of Science on 6/21/2021 10:31:09 AM.
- 108 S. Al-Jabour, M. Baer, O. Deeb, M. Leibscher, J. Manz, X. Xu and S. Zilberg, *J. Phys. Chem. A*, 2010, **114**, 2991–3010.
- 109 D. M. Charutz, R. Baer and M. Baer, *Chem. Phys. Lett.*, 1997, **265**, 629–637.
- 110 M. Baer, *J. Chem. Phys.*, 1997, **107**, 10662–10666.
- 111 M. Baer, S. H. Lin, A. Alijah, S. Adhikari and G. D. Billing, *Phys. Rev. A: At., Mol., Opt. Phys.*, 2000, **62**, 32506.
- 112 S. Adhikari, G. D. Billing, A. Alijah, S. H. Lin and M. Baer, *Phys. Rev. A: At., Mol., Opt. Phys.*, 2000, **62**, 32507.
- 113 B. Sarkar and S. Adhikari, *Int. J. Quantum Chem.*, 2009, **109**, 650–667.
- 114 B. F. E. Curchod and F. Agostini, *J. Phys. Chem. Lett.*, 2017, **8**, 831.
- 115 F. Agostini and B. F. E. Curchod, *Eur. Phys. J. B*, 2018, **91**, 141.
- 116 S. K. Min, F. Agostini, I. Tavernelli and E. K. U. Gross, *J. Phys. Chem. Lett.*, 2017, **8**, 3048.
- 117 M. Baer, *Mol. Phys.*, 1980, **40**, 1011.
- 118 M. W. Schmidt, K. K. Baldridge, J. A. Boatz, S. T. Elbert and M. S. Gordon, *et al.*, *J. Comput. Chem.*, 1993, **14**, 1347–1363.
- 119 M. J. Frisch, G. W. Trucks, H. B. Schlegel, G. E. Scuseria, M. A. Robb and *et al.*, *Gaussian 16 Revision C.01*, Gaussian Inc., Wallingford CT, 2016.
- 120 E. Baldini, T. Kubacka, B. P. P. Mallett, C. Ma, S. M. Koohpayeh, Y. M. Zhu, C. Bernhard, S. L. Johnson and F. Carbone, *Phys. Rev. B*, 2018, **97**, 125149.
- 121 N. N. Kovaleva, O. E. Kusmartseva, K. I. Kugel, A. A. Maksimov, D. Nuzhnyy, A. M. Balbashov, E. I. Demikhov, A. Dejneka, V. A. Trepakov, F. V. Kusmartsev and A. M. Stoneham, *J. Phys.: Condens. Matter*, 2013, **25**, 155602.
- 122 N. N. Kovaleva, O. E. Kusmartseva, K. I. Kugel and F. V. Kusmartsev, *J. Phys.: Conf. Ser.*, 2017, **833**, 012005.
- 123 J. Rodríguez-Carvajal, M. Hennion, F. Moussa, A. H. Moudden, L. Pinsard and A. Revcolevschi, *Phys. Rev. B: Condens. Matter Mater. Phys.*, 1998, **57**, R3189.
- 124 F. Cocchini, T. H. Upton and W. Andreoni, *J. Chem. Phys.*, 1988, **88**, 6068–6077.
- 125 A. K. Paul, S. Sardar, B. Sarkar and S. Adhikari, *J. Chem. Phys.*, 2009, **131**, 124312.
- 126 C. F. Jackels and E. R. Davidson, *J. Chem. Phys.*, 1975, **63**, 4672.
- 127 U. Kaldor, *Chem. Phys. Lett.*, 1991, **185**, 131–135.
- 128 E. Haller, H. Köppel and L. Cederbaum, *J. Mol. Spectrosc.*, 1985, **111**, 377–397.
- 129 R. Schinke, S. Y. Grebenschikov and H. Zhu, *Chem. Phys.*, 2008, **346**, 99–114.
- 130 M. Joyeux, R. Jost and M. Lombardi, *J. Chem. Phys.*, 2003, **119**, 5923–5932.
- 131 M. Sanrey and M. Joyeux, *J. Chem. Phys.*, 2006, **125**, 014304.
- 132 Y. Arasaki, K. Takatsuka, K. Wang and V. McKoy, *J. Chem. Phys.*, 2010, **132**, 124307.
- 133 Y. Arasaki, K. Wang, V. McKoy and K. Takatsuka, *Phys. Chem. Chem. Phys.*, 2011, **13**, 8681–8689.
- 134 S. Sardar, P. Puzari and S. Adhikari, *Phys. Chem. Chem. Phys.*, 2011, **13**, 15960.
- 135 S. Sardar and S. Adhikari, *J. Chem. Sci.*, 2012, **124**, 51.
- 136 B. A. Khan, S. Sardar, P. Sarkar and S. Adhikari, *J. Phys. Chem. A*, 2014, **118**, 11451.
- 137 S. Ghosh, T. Sahoo, S. Adhikari, R. Sharma and A. J. C. Varandas, *J. Phys. Chem. A*, 2015, **119**, 12392.
- 138 S. Mandal, S. Ghosh, S. Sardar and S. Adhikari, *Int. Rev. Phys. Chem.*, 2018, **37**, 607–700.
- 139 R. G. Sadygov and D. R. Yarkony, *J. Chem. Phys.*, 1999, **110**, 3639–3642.
- 140 R. de Vivie-Riedle, J. Gaus, V. Bonačić-Koutecký, J. Manz, B. Reischl-Lenz and P. Saalfrank, *Chem. Phys.*, 1997, **223**, 1–14.
- 141 R. Meiswinkel and H. Köppel, *Chem. Phys.*, 1990, **144**, 117–128.
- 142 H. Koizumi and I. B. Bersuker, *Phys. Rev. Lett.*, 1999, **83**, 3009–3012.
- 143 A. W. Hauser, C. Callegari, P. Soldan and W. E. Ernst, *J. Chem. Phys.*, 2008, **129**, 044307.
- 144 A. W. Hauser, C. Callegari, P. Soldan and W. E. Ernst, *Chem. Phys.*, 2010, **375**, 73.
- 145 G. Delacrétaz, E. R. Grant, R. L. Whetten, L. Wöste and J. W. Zwanziger, *Phys. Rev. Lett.*, 1986, **56**, 2598–2601.
- 146 M. Mayer, L. S. Cederbaum and H. Köppel, *J. Chem. Phys.*, 1994, **100**, 899–911.
- 147 M. Okumura, J. F. Stanton, A. Deev and J. Sommar, *Phys. Scr.*, 2006, **73**, C64.
- 148 J. F. Stanton, *J. Chem. Phys.*, 2007, **126**, 134309.
- 149 H. H. Nelson, L. Pasternack and J. R. McDonald, *J. Phys. Chem.*, 1983, **87**, 1286.
- 150 T. Ishiwata, I. Fujiwara, Y. Naruge, K. Obi and I. Tanaka, *J. Phys. Chem.*, 1983, **87**, 1349.
- 151 T. Ishiwata, I. Tanaka, K. Kawaguchi and E. Hirota, *J. Chem. Phys.*, 1985, **82**, 2196.
- 152 E. Hirota, T. Ishiwata, K. Kawaguchi, M. Fujitake, N. Ohashi and I. Tanaka, *J. Chem. Phys.*, 1997, **107**, 2829–2838.
- 153 A. Deev, J. F. Stanton and M. Okumura, *J. Chem. Phys.*, 2005, **122**, 224305.
- 154 T. Codd, M.-W. Chen, M. Roudjane, J. F. Stanton and T. A. Miller, *J. Chem. Phys.*, 2015, **142**, 184305.
- 155 S. Pancharatnam, *Proc. – Indian Acad. Sci., Sect. A*, 1956, **44**, 247.
- 156 M. V. Berry, *Proc. R. Soc. London, Ser. A*, 1984, **392**, 45.
- 157 H. Köppel, L. S. Cederbaum and W. Domcke, *J. Chem. Phys.*, 1988, **89**, 2023–2040.
- 158 S. Sardar, A. K. Paul, R. Sharma and S. Adhikari, *Int. J. Quantum Chem.*, 2011, **111**, 2741–2759.
- 159 S. Sardar, A. K. Paul, R. Sharma and S. Adhikari, *J. Chem. Phys.*, 2009, **130**, 144302.
- 160 S. Sardar and S. Adhikari, *J. Chem. Sci.*, 2012, **124**, 51–58.
- 161 P. M. Johnson, *J. Chem. Phys.*, 2002, **117**, 9991.
- 162 G. Bieri, L. Åsbrink and W. V. Niessen, *J. Electron Spectrosc. Relat. Phenom.*, 1981, **23**, 281–322.
- 163 G. Dujardin, S. Leach, O. Dutuit, T. Govers and P. M. Guyon, *J. Chem. Phys.*, 1983, **79**, 644–657.
- 164 D. A. Braden and B. S. Hudson, *J. Phys. Chem. A*, 2000, **104**, 982–989.
- 165 M. H. Palmer, W. Moyes, M. Spiers and J. N. A. Ridyard, *J. Mol. Struct.*, 1978, **49**, 105–123.

- Published on 20 October 2020. Downloaded by Indian Association for the Cultivation of Science on 6/21/2021 10:31:09 AM.
- 166 S. Adhikari and A. J. C. Varandas, *Comput. Phys. Commun.*, 2013, **184**, 270.
- 167 A. M. Mebel, G. J. Halász, A. Vibók, A. Alijah and M. Baer, *J. Chem. Phys.*, 2002, **117**, 991–1000.
- 168 T. Oka, *Phys. Rev. Lett.*, 1980, **45**, 531–534.
- 169 W. Meyer, P. Botschwina and P. R. Burton, *J. Chem. Phys.*, 1986, **84**, 891.
- 170 R. Röhse, W. Kutzelnigg, R. Jaquet and W. Klopper, *J. Chem. Phys.*, 1994, **45**, 753.
- 171 W. Cencek, J. Rychlewski, R. Jaquet and W. Kutzelnigg, *J. Chem. Phys.*, 1998, **108**, 2831.
- 172 K. Preston and J. C. Tully, *J. Chem. Phys.*, 1970, **54**, 4297–4304.
- 173 A. Kamisaka, W. Bian, K. Nobusada and H. Nakamura, *J. Chem. Phys.*, 2002, **116**, 654–665.
- 174 L. P. Viegas, A. Alijah and A. J. C. Varandas, *J. Phys. Chem. A*, 2005, **109**, 3307.
- 175 S. Adhikari and A. J. C. Varandas, *Comput. Phys. Comm.*, 2013, **184**, 270–283.
- 176 T. Sahoo, S. Ghosh, S. Adhikari, R. Sharma and A. J. C. Varandas, *J. Phys. Chem. A*, 2014, **118**, 4837–4850.
- 177 T. Sahoo, S. Ghosh, S. Adhikari, R. Sharma and A. J. C. Varandas, *J. Chem. Phys.*, 2015, **142**, 024304.
- 178 S. Ghosh, R. Sharma, S. Adhikari and A. J. C. Varandas, *Chem. Phys. Lett.*, 2017, **675**, 85–91.
- 179 L. P. Viegas, A. Alijah and A. J. C. Varandas, *J. Chem. Phys.*, 2007, **126**, 074309.
- 180 T. S. Chu and K. L. Han, *J. Phys. Chem. A*, 2005, **109**, 2050–2056.
- 181 T. S. Chu, A. J. C. Varandas and K. L. Han, *Chem. Phys. Lett.*, 2009, **471**, 222–228.
- 182 J. C. Polanyi and K. B. Woodall, *J. Chem. Phys.*, 1972, **57**, 1574–1586.
- 183 D. M. Neumark, A. M. Wodtke, G. N. Robinson, C. C. Hayden and Y. T. Lee, *J. Chem. Phys.*, 1985, **82**, 3045–3066.
- 184 D. M. Neumark, A. M. Wodtke, G. N. Robinson, C. C. Hayden, K. Shobatake, R. K. Sparks, T. P. Schafer and Y. T. Lee, *J. Chem. Phys.*, 1985, **82**, 3067–3077.
- 185 M. Faubel, L. Ruskin, S. Schlemmer, F. Sondermann, U. Tappe and J. P. Toennies, *J. Chem. Phys.*, 1994, **101**, 2106–2125.
- 186 R. T. Skodje, D. Skouteris, D. E. Manolopoulos, S. Lee, F. Dong and K. Liu, *J. Chem. Phys.*, 2000, **112**, 4536–4552.
- 187 C. F. Bender, S. V. O'Neil, P. K. Pearson and H. F. SchaeferIII, *Science*, 1972, **176**, 1412–1414.
- 188 C. F. Bender, P. K. Pearson, S. V. O'Neil and H. F. SchaeferIII, *J. Chem. Phys.*, 1972, **56**, 4626–4630.
- 189 J. T. Muckerman, *Theoretical Chemistry Advances and Perspectives*, Academic Press, New York, 1981, vol. 6A, p. 1.
- 190 T. Takayanagi and S. Sato, *Chem. Phys. Lett.*, 1988, **144**, 191–193.
- 191 S. L. Mielke, G. C. Lynch and D. G. Truhlar, *Chem. Phys. Lett.*, 1993, **213**, 10–16.
- 192 F. B. Brown, R. Steckler, D. W. Schwenke, D. G. Truhlar and B. C. Garrett, *J. Chem. Phys.*, 1985, **82**, 188–201.
- 193 K. Stark and H.-J. Werner, *J. Chem. Phys.*, 1996, **104**, 6515–6530.
- 194 B. Hartke and H.-J. Werner, *Chem. Phys. Lett.*, 1997, **280**, 430–438.
- 195 M. H. Alexander, D. E. Manolopoulos and H.-J. Werner, *J. Chem. Phys.*, 2000, **113**, 11084–11100.
- 196 G. Li, H.-J. Werner, F. Lique and M. H. Alexander, *J. Chem. Phys.*, 2007, **127**, 174302.
- 197 A. Das, D. Mukhopadhyay, S. Adhikari and M. Baer, *Int. J. Quantum Chem.*, 2012, **112**, 2561–2570.
- 198 A. Das, T. Sahoo, D. Mukhopadhyay, S. Adhikari and M. Baer, *J. Chem. Phys.*, 2012, **136**, 054104.